Implementation of an updated radiation stress formulation and applications to nearshore circulation

N. Kumar[1*], G. Voulgaris[1] and J.C. Warner[2]

---

[1]Department of Earth and Ocean Sciences
Marine Science Program
University of South Carolina
Columbia SC 29208,
USA
nkumar@geol.sc.edu; Ph: 803-777-4504; gvoulgaris@geol.sc.edu; Ph: 803-777-2549
[2]U.S. Geological Survey
Coastal and Marine Geology Program,
384 Woods Hole Road,
Woods Hole, MA 02543
USA
jcwarner@usgs.gov; Ph: 508-457-2237
[*]Corresponding Author

SUBMITTED

Abstract

Regional Ocean Modeling System (ROMS v 3.0), a three dimensional numerical ocean model, was previously enhanced for shallow water applications by including wave induced radiation stress forcing provided through coupling to wave propagation models (SWAN, REF/DIF). This enhancement made it suitable for surf zone environments and was demonstrated using applications like oblique incidence of waves on a planar beach and rip current formation in longshore bar trough morphology (Warner et al., 2008). In this contribution, we present an update to the coupled model which implements a revised method of the radiation stress term based on Mellor (2008) and a modification to that method to include a vertical distribution that is more appropriate for sigma coordinates in very shallow waters. The improvements of the updated model are shown through simulations of several cases that include: (a) obliquely incident spectral waves on a planar beach; (b) alongshore variable offshore wave forcing on a planar beach; (c) alongshore varying bathymetry with constant offshore wave forcing; and (d) nearshore barred morphology with rip-channels. Quantitative and qualitative comparisons to previous analytical, numerical and laboratory studies show that the updated model more accurately replicates surf zone recirculation patterns (onshore drift at the surface and undertow at the bottom) as compared to the previous formulation.

Keywords: wave-current interaction, rip currents, ROMS, radiation stress, SWAN, nearshore circulation

SUBMITTED

1. Introduction

Wave-induced circulation in the nearshore has been the subject of a number of experimental studies over the last 50 years. Theoretical and analytical studies were initiated in the 60s and 70s with the works of Longuet-Higgins and Stewart (1964), Longuet-Higgins (1970a, b) and Bowen (1969). These theories were later incorporated in numerical models that have been developed in the last 20 years. Such models are predominantly phase-averaged operating in 1-D (across the surf) or 2-D (assuming uniform along-coast bathymetry and depth-integrated). They solve the depth averaged Navier Stokes equation focusing on either simulating the development of alongshore currents (Church and Thornton, 1993; Stive and DeVriend, 1994; Feddersen et al., 1998; Ruessink et al., 2001), or rip current circulation (e.g., Yu and Slinn, 2003; Reniers et al., 2004a). Phase resolving 2-D Boussinesq models (e.g., Chen et al., 1999), although considered to be more comprehensive in modeling wave evolution in the nearshore, are computationally expensive and their use is limited at present. Lately, point-vortex models (Terrile et al., 2007; Kennedy et al., 2006) have been also used to study generation, maintenance and advection of breaking wave induced vortices which are associated with the formation of rip currents.

Overall 1-D and 2-D models provide useful information about circulation patterns but are intrinsically not able to resolve three-dimensional dynamics. It is imperative to resolve the 3-D circulation to fully investigate such processes as circulation dynamics for nearshore water quality applications, transport into and out of the surf zone, and sediment transport dynamics. In order to fill this need, initially quasi 3-D models like SHORECIRC (Svendsen et al., 2002) were developed. These models have been previously applied to study rip currents (Haas et al., 2003) and surf beat phenomena (van Dongeren et al., 1995) in nearshore environments. Lately, full 3-D wave-current coupled models have been developed and implemented in the coastal ocean

SUBMITTED

extending their application to the wave dominated environment of the surf zone. Implementations include use of the Generalized Lagrangian Mean (GLM) approach (Groeneweg and Klopman, 1998) to associate wave effects on currents as discussed by Walstra et al. (2000) and Lesser et al. (2004). Newberger and Allen (2007a, b) added wave forcing in form of surface stress and body forces in the Princeton Ocean Model (POM), which has evolved as "Nearshore POM". Using the vortex force formalism method described in McWilliams et al. (2004) and Craik and Leibovich (1976), Uchiyama et al. (2009) (hereafter referred to as U09) compares model simulations to field observations from a barred beach environment.

Mellor (2003, 2005) (hereafter referred to as M03 and M05, respectively) describes depth dependent formulation for radiation stress terms which has been implemented in ROMS by Warner et al. (2008, hereafter referred to as W08). This has been used to study oblique incidence of waves on a planar beach and rip currents formed on alongshore bar trough morphology (Haas and Warner, 2009; hereafter referred to as HW09). Following Ardhuin's et al. (2008a) remarks, Mellor (2008) (hereafter referred to as M08) modified his original formulation and provided a new approach for depth dependent radiation stresses. In this contribution, we present an implementation of the updated M08 formulations in the Regional Ocean Modeling System (ROMS) and provide both qualitative and quantitative comparisons for three and two dimensional flow fields corresponding to conditions favorable for the development of rip current cell circulation (see below).

The objectives of this contribution are to: (i) present the implementation of the updated M08 formulation, including further modifications to account for shallow water, into the ROMS model; and (ii) evaluate the performance of the new implementation using 4 study cases. These cases consist of: (1) obliquely incident waves on a planar beach; (2) uniform nearshore

SUBMITTED

bathymetry with alongshore varying wave forcing; (3) alongshore varying bathymetry with constant offshore wave forcing,; and (4) nearshore barred morphology with rip-channels.

The outline of the paper is as follows. Modifications to the model are presented in Section 2 together with the results for the case of obliquely incident waves on a planar beach (Case 1). Section 3 presents the results of the numerical experiments for the alongshore variable forcing, alongshore varying bathymetry and nearshore barred morphology with rip-channels (Cases 2, 3, and 4, respectively). The model results are compared to existing analytical solutions (Bowen, 1969), numerical solutions (Noda, 1974) and laboratory studies (Haller et al., 2002; Haas and Svendsen, 2002). Section 4 discusses the results with main emphasis on the effect of wave angle of approach to the development of rip-currents as it is revealed through the numerical experiments and some implications for model applications related to morphodynamic development. Finally, the conclusions are presented in Section 5.

2. Implementation of updated forcings

ROMS is a three dimensional, free surface, topography following numerical model, which solves finite difference approximations of Reynolds Averaged Navier Stokes (RANS) equations using hydrostatic and Boussinesq approximations with a split-explicit time stepping algorithm (Shchepetkin and McWilliams, 2005; Haidvogel et al., 2008; Shchepetkin and McWilliams, 2009). ROMS includes several options for certain model components such as various advection schemes (second, third and fourth order), turbulence closure models (e.g., Generic Length Scale mixing, Mellor-Yamada, Brunt-Väisälä frequency mixing, user provided analytical expressions, K-profile parameterization), boundary conditions etc.

SUBMITTED

Warner et al. (2008) improved ROMS for nearshore applications through the incorporation of the M03 and M05 radiation stress forcing methods. The model equations were presented inW08 in Cartesian coordinates (*x, y, s*) based on the equations originally given by Haidvogel and Beckmann (2000) and Haidgovel et al.(2008). Recently these formulations have been commented by Shchepetkin and McWilliams (2009) who presented clarifications to the model formulations. For completeness and to avoid confusion we elected to present the equations in horizontal, orthogonal curvilinear and vertical terrain following coordinates (ξ, η, s) following the definitions and notations of Shchepetkin and McWilliams (2009).

The horizontal momentum equations are given as:

$$
\begin{aligned}
&\frac{\partial}{\partial t}\left(\frac{H_z u_l}{mn}\right)+\frac{\partial}{\partial \xi}\left(\frac{u_l H_z u_l}{n}\right)+\frac{\partial}{\partial \eta}\left(\frac{v_l H_z u_l}{m}\right)+\frac{\partial}{\partial s}\left(\frac{w_s u_l}{mn}\right)- \\
&\left[\left(\frac{f}{mn}\right)+v_l\frac{\partial}{\partial \xi}\left(\frac{1}{n}\right)-u_l\frac{\partial}{\partial \eta}\left(\frac{1}{m}\right)\right]H_z v_l=-\frac{H_z}{n}\left(\frac{1}{\rho_0}\left.\frac{\partial P}{\partial \xi}\right|_z\right)-\frac{\partial}{\partial s}\left(\overline{u'w'}-\frac{\nu}{H_z}\frac{\partial u_e}{\partial s}\right) \\
&-\frac{\partial}{\partial \xi}\left(\frac{H_z S_{\xi\xi}}{mn}\right)-\frac{\partial}{\partial \eta}\left(\frac{H_z S_{\eta\xi}}{mn}\right)+s\frac{\partial}{\partial \xi}\left(\frac{H_z}{mn}\frac{\partial S_{\xi\xi}}{\partial s}\right)+s\frac{\partial}{\partial \eta}\left(\frac{H_z}{mn}\frac{\partial S_{\eta\xi}}{\partial s}\right)+\frac{H_z}{mn}\left(F_u+D_u\right)
\end{aligned}
\qquad [1]
$$

$$
\begin{aligned}
&\frac{\partial}{\partial t}\left(\frac{H_z v_l}{mn}\right)+\frac{\partial}{\partial \xi}\left(\frac{u_l H_z v_l}{n}\right)+\frac{\partial}{\partial \eta}\left(\frac{v_l H_z v_l}{m}\right)+\frac{\partial}{\partial s}\left(\frac{w_s v_l}{mn}\right)+ \\
&\left[\left(\frac{f}{mn}\right)+v_l\frac{\partial}{\partial \xi}\left(\frac{1}{n}\right)-u_l\frac{\partial}{\partial \eta}\left(\frac{1}{m}\right)\right]H_z u_l=-\frac{H_z}{m}\left(\frac{1}{\rho_0}\left.\frac{\partial P}{\partial \eta}\right|_z\right)-\frac{\partial}{\partial s}\left(\overline{v'w'}-\frac{\nu}{H_z}\frac{\partial v_e}{\partial s}\right) \\
&-\frac{\partial}{\partial \xi}\left(\frac{H_z S_{\eta\xi}}{mn}\right)-\frac{\partial}{\partial \eta}\left(\frac{H_z S_{\eta\eta}}{mn}\right)+s\frac{\partial}{\partial \xi}\left(\frac{H_z}{mn}\frac{\partial S_{\xi\eta}}{\partial s}\right)+s\frac{\partial}{\partial \eta}\left(\frac{H_z}{mn}\frac{\partial S_{\eta\eta}}{\partial s}\right)+\frac{H_z}{mn}\left(F_v+D_v\right)
\end{aligned}
\qquad [2]
$$

$$
-\left.\frac{\partial P}{\partial \eta}\right|_z=-g\left.\rho\right|_{s=0}\frac{\partial \varsigma}{\partial \eta}-g\int_s^0\frac{\partial \rho}{\partial \eta}H_z ds\,;-\left.\frac{\partial P}{\partial \xi}\right|_z=-g\left.\rho\right|_{s=0}\frac{\partial \varsigma}{\partial \xi}-g\int_s^0\frac{\partial \rho}{\partial \xi}H_z ds \qquad [3]
$$

with the continuity equation:

SUBMITTED

$$\frac{\partial}{\partial t}\left(\frac{H_z}{mn}\right)+\frac{\partial}{\partial \xi}\left(\frac{H_z u_l}{n}\right)+\frac{\partial}{\partial \eta}\left(\frac{H_z v_l}{m}\right)+\frac{\partial}{\partial s}\left(\frac{w_s}{mn}\right)=0 \qquad [4]$$

the scalar transport given by:

$$\frac{\partial}{\partial t}\left(\frac{H_z C}{mn}\right)+\frac{\partial}{\partial \xi}\left(\frac{u_e H_z C}{n}\right)+\frac{\partial}{\partial \eta}\left(\frac{v_e H_z C}{m}\right)+\frac{\partial}{\partial s}\left(\frac{w_s C}{mn}\right)= -\frac{\partial}{\partial s}\left(\overline{c'w'}-\frac{\nu_\theta}{H_z}\frac{\partial C}{\partial s}\right)+C_{source} \qquad [5]$$

and the Lagrangian velocity is related to Eulerian velocity (u_e) and Stokes drift (u_s) as:

$$u_l = u_e + u_s \qquad [6]$$

where m^{-1} and n^{-1} are Lamé metric coefficients; where u and v are the mean components of velocity in the horizontal (ξ and η) directions, respectively; subscripts l and e define Lagrangian and Eulerian velocity; w_s is the mean component of the vertical velocity in the vertical (s) direction. Note that no vertical Stokes velocity is defined in the Mellor (2008) method. The Lagrangian velocity in Eqn. 1-5 are replaced by Eqn. 6, and the terms corresponding to Stokes velocity are moved to right hand side of these equations. The ROMS model therefore solves for the Eulerian velocity as the prognostic variable. The vertical sigma coordinates $s=(z-\zeta)/D$ varies from -1 at the bottom to 0 at the free surface; z is the vertical coordinate positive upwards with z=0 at mean sea level; ζ is the wave-averaged sea surface elevation; D (= $h+\zeta$) is the total water depth while h is the depth below mean sea level of the sea floor; H_z is the grid cell thickness; and f is the Coriolis parameter. An overbar indicates time average, and prime (') indicates a fluctuating turbulent quantity. Pressure is P; ρ and ρ_0 are total and reference densities of sea water; g is the acceleration due to gravity; and ν and ν_θ are molecular viscosity and diffusivity; F_u and F_v are forcing terms (e.g., wind stress and thermal forcing, etc); C represents a tracer quantity; C_{source} are tracer source/sink terms; Finally, D_u and

SUBMITTED

D_v are diffusive terms (viscosity and diffusion) explained in details in the ROMS user guide (wikiROMS, www.myroms.org). For Cartesian coordinates (*x, y and s*) Lamé metric coefficients are unity and the curvilinear terms $(v_l\partial/\partial\xi(1/n)- u_l\partial/\partial\eta(1/m))$ reduce to zero.

These equations are closed by parameterization of the Reynolds stresses and turbulent tracer fluxes as:

$$\begin{aligned}&\overline{u'w'} = -K_M \frac{\partial u_e}{\partial z}, \overline{v'w'} = -K_M \frac{\partial v_e}{\partial z},\\ &\overline{c'w'} = -K_H \frac{\partial \rho}{\partial z}\end{aligned} \qquad [7]$$

where K_M is the eddy viscosity for momentum and K_H is the eddy diffusivity.

Ardhuin et al. (2008) pointed out that the implementation of depth dependent radiation stress equations described by M03 and M05 is not accurate and it requires inclusion of higher order wave kinematics. M08 attempted to address these issues and developed a modification to his original formulation for the radiation stress tensor:

$$S_{\alpha\beta} = kE\left(\frac{k_\alpha k_\beta}{k^2} F_{cs}F_{cc} - \delta_{\alpha\beta}F_{sc}F_{ss}\right) + \delta_{\alpha\beta}E_D \qquad [8]$$

where, k is the wave number and E the wave energy, while the parameter F denotes the vertical distribution defined as:

$$\begin{aligned}&Fss = \frac{\sinh k((s+1)(\zeta+h))}{\sinh k(\zeta+h)}, Fcs = \frac{\cosh k((s+1)(\zeta+h))}{\sinh k(\zeta+h)}\\ &Fsc = \frac{\sinh k((s+1)(\zeta+h))}{\cosh k(\zeta+h)}, Fcc = \frac{\cosh k((s+1)(\zeta+h))}{\cosh k(\zeta+h)}\\ &\delta_{\alpha\beta} = \begin{Bmatrix} 1 \text{ if } \alpha=\beta \\ 0 \text{ if } \alpha\neq\beta \end{Bmatrix}\end{aligned}$$

SUBMITTED

$$E_D = 0 \text{ if } z \neq \zeta$$
$$\int_{-h}^{\zeta} E_D dz = E/2 \qquad [9]$$

As described in M08, "*in a finite difference rendering of E_d, the top vertical layer of incremental size δz and only the top layer would be occupied by $\partial E_D/\partial\xi = (\delta z)^{-1}\partial(E/2)/\partial\xi$* "(hereafter this formulation is referred to as $M08_{top}$). This formulation is appropriate for cases where the discrete size of the top layer of the model is of the same order as or greater than the wave height. However, in very shallow waters as in the surf zone, the wave height is of the same order as the water depth. In such cases the amplitude of waves might be extending through a number of sigma levels ($H_{rms}/2>\delta z$). For this type of applications, if the forcing was applied only at the top layer, then the model result would be dependent on the vertical distribution of the sigma levels. In order to avoid this deficiency in shallow waters we vertically distribute the forcing using a function (F_{ED}) with a length that scales with the root mean square wave height (H_{rms}). We choose a distribution based on a function in Uchiyama et al. (2009):

$$F_{ED} = \frac{FB}{\int_{-h}^{\zeta} FB.dz} \text{ where, } \qquad FB = \cosh\left(\frac{2\pi}{H_{rms}}\left((s+1)(\zeta+h)\right)\right) \qquad [10]$$

so that equation (7) is implemented as:

$$S_{\alpha\beta} = kE\left(\frac{k_\alpha k_\beta}{k^2} F_{CS}F_{CC} - \delta_{\alpha\beta}F_{SC}F_{SS}\right) + \delta_{\alpha\beta}\frac{E}{2}F_{ED} \qquad [11]$$

and hereafter referred to as $M08_{vrt.}$. The $M08_{vrt}$ method provides a vertical distribution function such that the entire term E_D is not concentrated on the top sigma level. For cases when wave amplitude is smaller than the discrete interval of the top sigma level this approach is similar to $M08_{top}$.

SUBMITTED

Despite the modifications in Mellor (2008), some of the arguments of Ardhuin et al. (2008) remain valid for ideal conditions (i.e., high bed slope, non breaking waves propagating over uneven topography with no dissipative effects). In order to assess the error of Mellor (2008) as implemented in this work, an analysis was carried out for a similar setup as Ardhuin et al. (2008) but with a realistic slope and including bottom friction and uniform vertical mixing (see Appendix A). The results indicate that under the latter conditions the errors are not significant when compared to the flow field developed by depth induced wave breaking.

In addition to the radiation stress term, spatial distribution of wave energy is affected by wave breaking process. This is usually incorporated through the inclusion of wave rollers (e.g., Ruessink et al., 2001) that modify the radiation stress and associated alongshore and cross-shore velocities. A formulation for these processes was already incorporated in ROMS using an empirical parameterization (Warner et al., 2008). A new formulation based on the evolution equation of roller action density (Reniers et al., 2004) is currently being developed. However, in this manuscript no roller effects are included and this is the subject of a subsequent publication.

The wave fields required to compute the radiation stress terms are provided by SWAN (Booij et al., 1999), a third generation, phase averaged, wave propagation model, which conserves wave action density (energy density divided by relative frequency). The details of coupling ROMS to SWAN have been provided in W08 and will not be discussed further in here.

2.1 Case 1: Obliquely incident waves on a planar beach

The effects of updated forcing methods are examined through simulations for obliquely incident waves on planar beach. This case has been previously discussed by HW09 using the M03 formulation. The model domain has a cross-shore width (x) of 1,180 m and an alongshore

SUBMITTED

length (y) of 140 m. The grid resolution is 20 m for both directions. The water depth varies from 12 m at the offshore boundary to 0 m at the shoreline. The vertical domain has been distributed in 30 vertical layers. The boundary conditions are periodic in the alongshore (i.e., north and south boundaries), closed at the shoreline, and Chapman like radiation condition at the offshore end of the domain. Effect of earth rotation has not been included. The bottom stress has been formulated using a quadratic bottom drag with a C_d value of 0.0015. The turbulence closure scheme is Generic Length Scale (GLS, k-epsilon) as described in Warner et al. (2005). For this simulation, wave forcing is provided by SWAN, which propagates an offshore JONSWAP wave spectrum with a significant wave height of 2m, a peak period of 10 seconds and a 10° angle of incidence.

U09 conducted similar tests on the same setup using the vortex force formalism (McWilliams et al., 2004) to compute the wave forcings. Results were compared to those in HW09, which was based on the original vertical distribution of M03. Here we compare the vertical structure of cross-shore velocity between M03 and the present model using both $M08_{top}$ and $M08_{vrt}$ in order to reveal the differences between the older and newer formulations, but also to examine the performance of the radiation stress vertical distribution shown in Eqn. 10.

The cross-shore distribution of wave height, water depth and sea surface elevation after 6 hours of model simulation time are shown in Figure 1a. The free surface is very close to zero at the offshore boundary and gradually decreases landward with a maximum setdown at x=560m. The waves start breaking at x > 560 m as determined by wave setdown and reduction in wave height. A comparison of the depth averaged, cross-shore and alongshore Eulerian velocities for the different simulations (i.e., M03, $M08_{top}$ and $M08_{vrt}$ formulations) are shown in Figures 1b and c. The cross-shore profile of the depth-averaged cross-shore velocity (Fig. 1b) is identical for all

SUBMITTED

three simulations with the maximum current occurring at 700m. On the other hand, the strength of the maximum depth averaged alongshore velocity (Fig. 1c) for $M08_{top}$ and $M08_{vrt}$ is slightly weaker in comparison to M03. This reduction in alongshore velocity in $M08_{top}$ and $M08_{vrt}$ is compensated for by an increase in alongshore velocity further offshore from the shoreline.

The vertical structure of the cross-shore Eulerian velocity at five different locations across the shoreface and for each simulation is shown in Figure 2. At the furthest offshore location (x=100 m), the M03 cross-shore velocity profile shows offshore directed velocity increasing in strength from 0 ms^{-1} at z=-4 m to 0.15 ms^{-1} at z=-10.5 m. For z>-4 m, the velocity is directed onshore with maximum strength at the surface layer. At the same location, the $M08_{vrt}$ results show no velocity at the surface, increasing towards the bed with offshore directed velocity of 0.15 ms^{-1}. The $M08_{top}$ simulations are similar to those of $M08_{vrt}$ except near the surface, where offshore velocity of 0.10 ms^{-1} is observed at the surface layer. The velocity profile at x=300 m follows similar trend as before for M03 and $M08_{vrt}$, while for $M08_{top}$ offshore advection at the surface layer is observed with a velocity of the order ~0.2 ms^{-1}.

At the location just offshore of the wave breaking zone (i.e., x=500 m), M03 runs have maximum offshore directed velocity (~ 0.2 ms^{-1}) at the bottom layer which decreases to 0 at the surface. For $M08_{top}$ run, strongest offshore flow is at the bottom layer which decreases to a magnitude ~0.1 ms^{-1} at z=0 m. The velocity profile from $M08_{vrt}$ run has maximum offshore velocity at z=-6 m with a strength of ~0.2 ms^{-1}, reducing to ~0.05 ms^{-1} at the surface.

Within the surf zone (x>500 m), the original model (M03) run predicts a strong offshore directed velocity near the bed. At the surface, the velocity is still directed offshore but with a significantly reduced strength. The $M08_{top}$ and $M08_{vrt}$ results are very similar within the surf zone. Close to the bottom boundary, velocity is directed offshore with a higher value than that

SUBMITTED

observed for the M03 run. Near the surface, velocity is directed onshore as expected in the surf zone while an offshore directed undertow is developed near the bottom (also see Fig. 1, in Longuet-Higgins, 1953). This vertical segregation of flow leads to the development of a cross-shore circulation cell with a vertical velocity (not shown here) directed upwards at x~500 m and downwards close to the shoreline at x~900 m. This is generally consistent with field observations of cross-shore velocity profile within the surf zone that show similar vertical flow segregation for both barred (Garcez-Faria et al., 2000) and non-barred planar beaches (Ting and Kirby, 1994).

Overall, the M03 formulation predicts onshore velocity for areas outside the surf zone and fails to reproduce the recirculation pattern within the surf zone. The M08 based simulation with stress applied to top layer ($M08_{top}$) works well within the surf zone but creates weak offshore advection of cross-shore velocity near the surface. However this offshore advection is eliminated when, implementing Eq. 10 ($M08_{vrt}$). Furthermore, at the breaking zone the $M08_{vrt}$ model results are qualitatively in agreement with the field observations of Garcez-Faria et al. (2000) that show slight onshore flow near the surface and offshore flows below increasing with proximity to the bed (see Fig. 1c in Garcez-Faria et al., 2000).

3. Nearshore Circulation Cell Cases

Rip currents have been the subject of modeling (Bowen et al., 1969b; Tam, 1973; Noda, 1974; Dalrymple, 1975; Haas et al., 2000; Haller et al., 2001; Haas et al., 2003) but also experimental studies in both the field (MacMahan et al., 2005; Aagaard et al., 1997; Brander and Short, 2001; Sonu, 1972), and the laboratory (Haller et al., 2002; Drønen et al., 2002). They provide a good example for testing nearshore numerical models as they invoke a number of nearshore processes and wave and current interaction patterns. In this section we have applied

SUBMITTED

the $M08_{vrt}$ formulation and examine its performance on rip current development by comparing to previously published work.

Initially, two ideal cases are presented where rip current cells develop in response to alongshore variability of wave forcing (Case 2) and alongshore variable bottom bathymetry (Case 3). The former condition can be the result of temporal variability in wave group forcing (e.g., Long and Özkan-Haller, 2009) or due to incidence of intersecting wave trains of similar frequency (e.g., Dalrymple, 1975). On the other hand, the latter condition is not uncommon in barred beach profiles. In each case, alongshore differences in wave setup, caused by alongshore variation of the wave breaking position, create an alongshore pressure gradient which in turn drives an alongshore current. In both cases the creation of alongshore gradient in wave setup leads to the development of a circulation cell like pattern in the surf zone as described in Bowen (1969) and Noda (1974).

In addition, the laboratory studies of rip currents by Haller et al. (2002) are well documented and provide an excellent set of data for comparison to numerical model results. HW09 provided a qualitative comparison of rip current formation to results from Haller et al. (2002). Expanding on this previous work we use the updated model to simulate the formation of rip currents on an alongshore bar trough morphology (Case 4) which is a scaled up experiment of the laboratory study conducted by Haller et al. (2002) and Haas and Svendsen (2002).

3.1 Case 2: Alongshore variable wave forcing.

The setup of this case study includes incidence of alongshore variable wave height distribution on a planar beach as described by Bowen (1969). Our case differs from Bowen's

SUBMITTED

setup as we use spectral instead of monochromatic waves and the domain size has been increased to resemble realistic field conditions.

The alongshore uniform, planar bathymetry is analytically described by:

$$d = \tan \beta \cdot x \cdot \left(1 + \varepsilon \cdot \cos \lambda y\right) \qquad [12]$$

For $\varepsilon << 1$, this can be approximated as $d \approx \tan \beta x$. The beach slope $\tan\beta$ is 0.02 and the water depth (d) varies from 12 m offshore to 0 m close to the shoreline. The domain is 650 m in the cross-shore and 1,000 m in the alongshore direction, with a resolution is 5 and 10m, respectively. In the following discussion, results only from the area 600m (x from 0m to 600m) by 1000m (y from 0 to 1000m) is shown, so that boundary effects are excluded. Vertically, the domain is distributed in 10 equally distributed sigma layers. Closed boundary conditions are used at the two lateral sides and the shoreline, while Neumann boundary conditions have been used at the offshore boundary. A logarithmic bottom friction is used with a roughness length of 0.005 m, a value close to those reported from field studies (e.g., Feddersen et al., 1998).

The wave model (SWAN) is run for the same grid as ROMS. The wave forcing applied at the offshore boundary is directed perpendicular to the domain, has a period of 5 s and an alongshore varying wave height described (see eqn. 30, 31 in Bowen, 1969) by:

$$H = \gamma \cdot \frac{(1 - \mathrm{K})\tan\beta}{f} \cdot x \cdot \left(1 + 0.2 \cdot \cos(\lambda y)\right) \qquad [13]$$

where λ is the alongshore wavenumber of the wave height variability ($2\pi/L_y$, with L_y=1,000m), f is a scaling constant, $\tan\beta$ is the beach slope, K (a parameter which relates wave setup to slope) is calculated as $(1 + 8/3\gamma^2)^{-1}$ and γ (=0.6) is the depth-induced wave breaking constant (Battjes and Janssen, 1978; Eldeberky and Battjes, 1996). The wave forcing is described by a directional spectrum consisting of 20 frequency bands in the range 0.04 Hz to 1 Hz, and 36 directional bins of 10° each from 0° to 360 with a directional spreading of 6°. The bottom friction used in SWAN

SUBMITTED

is based on the eddy viscosity model of Madsen et al. (1988) with a bottom roughness length scale of 0.05 m. The modeling system for this case is configured in one way coupling where there is no feedback of the currents or water levels to the wave model, and in a two way-coupling mode where exchange of wave and current information takes place between ROMS and SWAN at a synchronization interval of 20s. Both model configurations were run for a simulation time of two hours over which the computational domain achieves stability. Unlike Yu and Slinn (2003) very small differences were observed between the final results of one and two way coupling based simulations. We attribute this to a number of reasons including differences in wave forcing, bottom friction values and on the width of the rip current jet in the two cases. As Yu and Slinn (2003) mention the current effect on waves is stronger for narrow offshore rip currents as in their case, while in the present study the rip system is approximately 250 m wide. In the following sections we discuss the two way coupled results unless otherwise mentioned.

The wave height distribution over the domain is shown in Figure 3. The wave incident at the offshore boundary is alongshore variable with a maximum value of 1.5 m at the lateral boundaries and a minimum value of 1 meter at the center of the domain. At the center of the domain (i.e., $\lambda y= \pi$), the incident wave height initially decreases and then increases before it starts breaking in shallower water depths. The initial decrease is due to bottom friction and depth induced dissipation and the increase after that is due to interaction of the incoming wave field with the outgoing currents. This outgoing current locally increases the wave height by a small value (0.05-0.10 m).

The depth averaged Lagrangian (Eulerian + Stokes) velocity and the associated streamlines are compared to analytically derived streamlines - following Bowen (1969) - assuming a breaking position of $\lambda x=\pi/2$ (Fig. 4). The flow patterns are symmetrical about $\lambda y= \pi$,

SUBMITTED

therefore only the bottom half is shown and discussed here. The flow pattern within the surf zone ($\lambda x<\pi/2$) is onshore, offshore and alongshore directed at $\lambda y=0$, π, $\pi/2$ respectively. The alongshore current within the surf zone increases from 0 to 0.2 ms^{-1} and then reduces to 0 ms^{-1} at $\lambda y= \pi$. For locations outside the breaking zone ($\lambda x>\pi/2$), the alongshore current is relatively weaker and is directed from $\lambda y= \pi$ to $\lambda y=0$. Within the surf zone the streamline patterns observed are similar for both the analytical solution (Fig. 4c) and the model simulation (Fig. 4b). It is important to note that longshore symmetry of streamlines about the center of circulation is observed which suggests that the strength of offshore and onshore directed flow at $\lambda y=0$ and $\lambda y = \pi$ are of the same magnitude. Outside the surf zone (i.e., for $\lambda x>\pi/2$), the two streamline patterns differ. The model based streamlines show uniform distribution pointing at equal strength of alongshore and cross-shore velocity from $\pi/2 < \lambda x < 6\pi/5$. The analytical solution (Fig 4c) suggests reduction in velocity when moving further offshore (seen by increase in distances between the corresponding streamlines). These differences occur because the analytical solution includes only bottom friction as a parameter for dissipation whereas the model simulations include additional dissipative and mixing processes which make the velocity distribution uniform outside the surf zone. Overall even though we use different bottom friction, turbulence closure schemes etc., qualitatively the results are comparable to Bowen 1969 (their Fig. 6) and to the results of LeBlond and Tang (1974) who included wave-current interaction in their analytical solution.

In order to examine the effect of lateral mixing on circulation pattern, we implement a sensitivity analysis based on a Reynolds Number defined as VL_y/A_H, where V is the maximum alongshore velocity speed, L_y is the alongshore wavelength of the forcing perturbation and A_H is the horizontal coefficient of viscosity (Fig 5). Small changes in bottom friction affect the

SUBMITTED

maximum velocity value but not the circulation pattern (not shown here). On the other hand, changes in horizontal mixing, affect both velocity strength and circulation pattern. As the Reynolds number increases, the solution becomes more skewed, i.e., outflowing current at the location of lower waves tends to become narrow and the onshore flow broadens. This effect is shown in Fig. 5 where the stream function for different values of Reynolds number is presented. As A_H decreases from 6 to 0.5, the Reynolds Number increases from 42 to 500, making the solution more skewed about the individual circulation cell centers. Qualitatively this solution compares well to both theory of Arthur (1962) and the results derived by Bowen (1969) by numerically solving the non linear problem for streamline distribution.

The vertical structure of the cross-shore and alongshore Eulerian velocities along three profiles at $\lambda y=\pi/5$, $\pi/2$ and $4\pi/5$ (for locations see Fig. 3), corresponding to locations where the depth averaged cell flow is directed onshore, alongshore and offshore, respectively, are shown in Fig. 6, respectively. These results correspond to simulation runs with A_H=0.5 m^{2}s^{-1}. The first location (Fig. 6a) corresponds to bigger waves which start breaking further offshore (λx~0.5π). The region onshore of location $\lambda x=0.5\pi$, shows a vertical segregation of the flow. The onshore flow observed at the surface layer at $\lambda y= \pi/5$ (Fig. 6a) is stronger than the surface onshore flow at $\lambda y= \pi/2$ (Fig. 6b). Presence of a circulation pattern in the domain reinforces current directed towards the shoreline at $\lambda y=\pi/5$. The offshore flow in this case is weak and is limited to the bottom boundary. The vertically integrated flow is directed onshore as shown in Fig 4a. Outside the surf zone (i.e., $\lambda x>0.5\pi$), the flow is predominantly weak, onshore directed (~0.05 ms^{-1}) at the upper half of the sigma layers and gradually decreases to no flow at the bottom layer (Fig 6a).

SUBMITTED

At the third vertical profile (Fig. 6c), the incoming waves are small and break close to the shoreline ($\lambda x \sim 0.4\pi$). The flow field close to the surface is weakly (<0.05 ms^{-1}) onshore directed as this velocity at the surface is reduced by the rip current jet directed offshore. Also the onshore flow is limited to the top layer. The offshore directed undertow is stronger in this case and occupies the largest part of the water column. The vertically averaged flow is strongly offshore directed. Outside the wave breaking zone (i.e. $\lambda x > 0.4\pi$) the velocity strength steadily decreases from 0.2ms^{-1} to 0.05 ms^{-1}.

Panels d, e, and f, in Fig. 6, show the vertical structure of alongshore velocity at the same locations as in Figs. 6a, b and c, respectively. At $\lambda y = \pi/5$ (Fig. 6d), alongshore velocity within the surf zone ($\lambda x < 0.45\pi$) has a strength of 0.1 ms^{-1} while at $\lambda y = \pi/2$ (Fig. 6e), velocity is positive and strongest (0.2 ms^{-1}) at the surface, gradually decreasing to 0.15 ms^{-1} near the bed. This is reflected in the strong depth averaged alongshore velocity observed within the surf zone in Fig. 4a. At $\lambda y = 4\pi/5$ (Fig. 6f), velocity within the surf zone is stronger than that at $\lambda y = \pi/5$. This occurs because the streamlines in this case are not symmetrical about the center of the circulation (Fig. 5a) and the offshore flow occurs over a smaller area in comparison to broadened onshore flow. Offshore of $\lambda x = 0.45\pi$ (outside the surf zone), the alongshore flow is small and gradually increases to -0.10 ms^{-1} for rest of the vertical domain for $\lambda y = \pi/5$, $\pi/2$ and $4\pi/5$.

3.2 Case 3: Alongshore Varying Bathymetry

In this case study the alongshore bathymetry of the beach is varied to produce a sinusoidal pattern according to (Noda, 1974):

$$d(x,y) = \tan\beta \cdot x \cdot \left(1 + a \cdot \exp\left(-\left(\frac{x}{(\alpha/3)}\right)^{1/3}\right) \cdot \sin^{10}\left(\frac{\pi y}{L_y}\right)\right) \qquad [14]$$

SUBMITTED

where the beach slope ($tan\beta$) is 0.025, the wavelength(L_y) of the alongshore variation is 80m and α is a constant (20). This analytical expression generates a periodic beach bathymetry with channels concentrated at alongshore distances multiples of L_y while it produces a straight coastline at x=0 m.

The numerical model domain is 110m and 560m in the cross-shore and alongshore directions, respectively with a resolution of 2 m in both directions. Application of Eqn. 14 over the domain generates 7 channel-like features. In the following discussion, results only from the central feature, over an area 100m (x from 0m to 100m) by 80m (y from 240 to 320m) is shown, so that boundary effects are excluded. Ten equally spaced sigma layers were used in the vertical. Closed boundary conditions are implemented in the lateral and coastline and Neumann conditions at the offshore boundary. Logarithmic bottom friction has been implemented with a roughness length of 0.005 m.

The same grid is used by the SWAN wave model and the wave forcing is a directional spectrum as that used in Case 2 but with a directional spreading of 2°. Wave conditions are similar to those used by Noda (1974) with a significant wave height 0.92 m, peak wave period 4 s and normally incident at the offshore boundary. The other variable parameters are same as in Case 2 (i.e., depth induced breaking constant, γ=0.6 and bottom friction with roughness length of 0.05m). The ROMS-SWAN system in this case is operated in a two way coupling mode, exchanging wave current information at a 20s interval. The results presented here are after 1 hour of simulation when the model has achieved stability.

The depth-averaged Eulerian velocity and wave height distribution are shown in Figs. 7a and b, while the vertical distribution of the cross-shore current for two transects corresponding to y=240 and 280 m are shown in Figs. 7c and d. The results indicate the development of rip

SUBMITTED

currents and the interaction of the waves with the bathymetry which is exhibited as alongshore differences in wave breaking position (not shown in here). In addition, it is characteristic that the wave height slightly increases over the area of the rip current development (see cross-shore locations 60 to 80 m) due to the interaction of strong outgoing current with the incoming waves.

The vertical profile of cross-shore Eulerian velocity at the transect located at y=240 m is shown in Fig. 7c. Wave breaking starts at x=70 m as determined by a vertical shear observed in the cross-shore velocity profile. Further offshore (x > 70 m), the entire water column shows an onshore directed velocity due to the background circulation pattern observed in the domain (Fig. 7a). In a normal surf zone circulation pattern (see Case 1, Fig. 2) onshore flow is observed near the surface. This onshore surface flow is further enhanced in this case due to the presence of the onshore component of the circulation cell . The offshore flow is limited to elevations close to the bottom boundary other than in very shallow waters (z<-0.5 m), where the entire water column is directed offshore. The vertical profile of cross-shore velocity at y=280 m is depicted in Fig. 7(d). Wave breaking takes place at 1.5 m depth; some 60 m from the shoreline (see Fig. 7b). The rip current strength is approximately 0.5 ms^{-1} and is strongest at the bottom layer gradually reducing on moving up the water column. In shallow waters (1 m) rip current strength decreases and close to the shoreline a vertical shear in velocity is observed. The vertical structure of the cross-shore flow at y=0 and 40 m is similar to that at locations $\lambda y= \pi/5$ and $4\pi/5$ respectively for Case2 and are shown in Fig. 6a and 6c.

The normalized stream function calculated using the depth averaged Lagrangian velocities from the model output is shown in Fig. 8 together with the stream function generated by Noda (1974). In both cases the streamlines converge at y=40m, creating a flow pattern from shallower to deeper waters, simulating a rip current like situation. The maximum value of stream

SUBMITTED

function occurs close to x=60 m for Noda (1974) and x=70 m for our simulations. Both results are almost symmetrical around line y=40m. It is worth noticing that our system of stream function is shifted slightly to the right in comparison to Noda (1974).

The depth averaged cross-shore velocity in the rip channel is approximately 0.5 ms^{-1} (Fig. 7a), a value more reasonable than that of Noda (1974), where for the same setting he predicted a rip current velocity in excess of 4 ms^{-1}. The differences in distribution of stream function and magnitude of rip current velocity occurs because, as acknowledged by Noda (1974, see pp. 4105), his depth averaged model was rather simplified as it only accounts for pressure gradient, radiation stress and bottom friction and does not account for current-induced wave refraction and modifications of the wave field due to Doppler shift, as in the present model. Furthermore, the unrealistic rip current velocity predicted by Noda (1974) implies that the stream function might not be accurate enough for direct comparison with our model which seems to give more realistic results.

3.3. Case 4: Comparison to Scaled Laboratory Studies

This case study investigates the dynamics for a barred beach bathymetry that develops rip currents. The application is based on a laboratory scale experiment and is similar to a case demonstrated in HW09. However there are two major differences: (i) in HW09 the wave driver was a monochromatic wave model (REF/DIF), while here we use a spectral wave model (SWAN); and (ii) the domain used in HW09 was identical to the laboratory experiments while in our simulations the domain has been scaled by a factor of 10 (kinematic similarity, Hughes, 1993) to create more realistic field conditions.

SUBMITTED

The bathymetry domain (Fig. 9) is an idealized version of that used by Haller et al. (2002) and Haas and Svendsen (2002). The scaling of the domain by a length scale, N_L= 10 lead to a maximum depth of 5 m, a nearshore bar of 0.60 m located 40m off the coastline, cross-shore domain width of 146 m and alongshore length of 262 m. To avoid interaction of rip channel flow with the lateral boundaries, the domain was extended laterally by 40m in either direction. Rip channels are spaced 92 m apart and the channel width is 18.2 m which makes the ratio of channel width to rip current spacing 0.2, a value consistent with those found in the field (e.g., Huntley and Short, 1992; Aagaard et al., 1997, Brander and Short, 2001). The model grid has a horizontal resolution of 2 m in both directions and consists of 8 equally spaced sigma layers. The boundary conditions at shoreline, offshore boundary and lateral ends are no flow conditions (i.e., closed boundary conditions at the coast, lateral boundaries and offshore) and same as the laboratory experiments of Haller et al., (2002). Bottom friction (bottom roughness of 0.015m) similar to that of HW09 is used in our work. Our simulations were carried out with both the updated vertical distribution (Eqn. 10) of the radiation stress ($M08_{vrt}$, see section 2) and the original version (M03) used in HW09.

At the offshore boundary, SWAN was forced with 0.5m waves with peak period of 3.16 s, and directional spreading of 3° propagating perpendicular to the shoreline. From these values SWAN computes a wave spectrum based on a JONSWAP distribution. The spectral resolution is 20 frequency bands in the frequency range between 0.04 Hz and 1 Hz, and 36 directional bins of 10° each from 0° to 360°. The other variable parameters are same as in Case 2 and 3 (i.e., depth induced breaking constant, γ=0.6 and bottom friction with roughness length of 0.05m). The time stepping used for ROMS and SWAN are 2 and 10 seconds respectively and the coupling between the models take place at 20 s intervals. Initial comparisons are done only for 30 minutes

SUBMITTED

of simulation time. The model remains stable because we use a higher bottom friction coefficient and horizontal mixing than typically observed in field.

The wave height distribution over the domain using the original and newer version of ROMS (i.e., M03 and $M08_{vrt}$ formulations, respectively) is shown in Fig.10a & b. At the location of rip channel, the increase in wave height due to offshore directed rip current is lower in the $M08_{vrt}$ than the M03 simulations. The waves propagating over the bar break and generate a higher wave setup than the setup generated by waves propagating over the channel. This creates feeder currents moving from the bar towards the channel. Waves approaching the shoreline over the channel become steeper, decrease in wavelength and increase in height due to interaction with the rip current. These bigger waves break close to the shoreline creating alongshore currents which move away from the channel at shallow depths. This phenomenon can be further confirmed by comparing the mean sea surface elevation over the bar and channel for $M08_{vrt}$ based simulations (Fig.11). The elevation is lower at the location of the channel than over the bar. On the other hand, closer to the shoreline the sea surface at the channel location is higher than over the bar driving the observed flow patterns.

M03 derived depth averaged, Eulerian cross-shore velocity (see Fig. 10c & d) at the channel is 25% stronger than that predicted by the updated $M08_{vrt}$. The stronger offshore directed velocity locally creates a greater increase in wave height at the location of rip channel in M03. Further offshore of the rip channel, the magnitude of cross-shore velocity is similar in both M03 and $M08_{vrt}$ and hence the wave height pattern is also similar. The primary circulation pattern with feeder currents exiting through the rip channel and return flow over the bar is evident irrespective of the formulation used. These circulation cells are symmetric both with respect to the rip channel and about the axis of the alongshore bar.

SUBMITTED

Noticeable differences in secondary circulation pattern for M03 and $M08_{vrt}$ based simulations can be seen in Fig. 10 (c & d). Waves with greater wave height at the vicinity of the rip channel, for M03 formulations, drive a larger setup and stronger alongshore pressure gradient close to the shoreline in comparison to $M08_{vrt}$ formulations. As a consequence the secondary circulation pattern close to the shoreline is stronger for the M03 than the $M08_{vrt}$ based simulations.

The vertical variability of cross-shore Eulerian velocity at the center of the channel is shown in Figures 12a & b for M03 and $M08_{vrt}$, respectively. Inshore of the bar location wave breaking induces onshore directed velocity at the surface extending all the way to the bed for M03 (Fig. 12a), while for the $M08_{vrt}$ simulation a return flow develops near the bed (Fig. 12b). Over the bar and shoreward the cross-shore flow structure differs between the two simulations (Figs. 12c & d). The M03 simulation (Fig. 12c) shows the development of offshore flow throughout the water column, while the improved model simulation results in an onshore flow near the sea surface with a stronger return flow near the bed. Further offshore both simulations give similar results. These findings, show that the incorrect vertical distribution of the radiation stress in M03 fails to create a surf zone vertical recirculation system, while the $M08_{vrt}$ run provides more realistic results that show qualitative agreement to field observation of cross-shore velocity profile for barred beaches (see Fig. 1c, Garcez-Faria et al., 2000).

Our scaled numerical experiment conditions correspond to Test B of Haller et al. (2002) and Test R of Haas and Svendsen (2002). Thus, we use the results of those lab experiments to provide semi- quantitative comparison between the measured and modeled vertical structure of the cross-shore velocity field. For this comparison we use all of the bin averaged velocities from Test R (Fig. 11, Haas and Svendsen, 2002) and for all reported locations (Fig. 12e). The

SUBMITTED

measured and model calculated velocities are normalized by the maximum cross-shore velocity measured and modeled at the bar crest (i.e. x=27m, Fig. 12e), respectively. The simulated normalized cross-shore current vertical structure from the upgraded model agrees well with the experimental data. Inside the channel, rip current speed is maximum at the level of the bar crest and decreases toward the surface and bed. However no experimental data are available near the surface. Just off the bar, the normalized data show the best agreement with our simulation using $M08_{vrt}$. Such a relative agreement between data and model persists in areas further offshore of the bar location.

For steady flow the depth and time averaged cross-shore (x) momentum equation can be written as:

$$\frac{\partial}{\partial x}\left(U^2 h\right)+\frac{\partial}{\partial y}\left(U.V.h\right)=-gh\frac{\partial \eta}{\partial x}-\frac{1}{\rho}\left(\frac{\partial S_{xx}}{\partial x}+\frac{\partial S_{xy}}{\partial y}\right)-\frac{\partial}{\partial x}\left(A_H\frac{\partial U}{\partial x}\right)-\frac{\tau_x^b}{\rho} \qquad [15]$$

where U and V are the depth averaged cross and along shore Lagrangian velocities, respectively, h is the total depth, ρ is the fluid density, S_{ij} represents the components of the radiation stress tensor, τ_x^b is the component of the bottom stress acting in the x-direction and A_H is the horizontal viscosity coefficient.

Since the depth averaged distribution of these terms is same for both the original and updated model, only results from the latter are shown here (Fig. 13). Alongshore variation of the depth averaged horizontal advection, bottom friction terms and gradient of alongshore radiation stress ($\partial S_{xy}/\partial y$) in the cross-shore direction, are shown in Fig. 13a-d for four locations (40, 30, 26 and 20 m respectively from the shoreline, see Fig. 9). Since horizontal advection and bottom stress depend on velocity magnitude and gradients, these terms become important within and in the vicinity of the rip channel as seen in Fig. 13(b & c). Close to the shoreline and further offshore, bottom friction and horizontal advection become less significant. For normally incident

SUBMITTED

waves S_{xy} and $\partial S_{xy}/\partial y$ should be 0 at all the locations, as is observed in Fig. 13 (a, b, c and d) for all alongshore positions other than the rip channel. Local wave refraction effects due to interaction of rip currents with incoming waves lead to the development of $\partial S_{xy}/\partial y$ within the rip channel. These terms are partially in balance with the horizontal advection terms, at locations within and outside the rip channel area as shown in Fig. 13(a, b and c). $\partial S_{xy}/\partial y$ becomes relatively insignificant very close to the shoreline (Fig. 13d).

The alongshore variation of depth averaged horizontal viscosity, pressure gradient and radiation stress at the same transect locations as for the other terms (see above) are shown in Fig. 13e-h. At distances 40m from the shoreline, where no wave breaking occurs, the gradient of cross-shore radiation stress ($\partial S_{xx}/\partial x$) and pressure gradient terms are insignificant. Within the surf zone, $\partial S_{xx}/\partial x$ is balanced by the pressure gradient for all alongshore locations (Fig. 13 f, g and h). As wave breaking initiates at the bar crest, $\partial S_{xx}/\partial x$ is weaker within the rip channel (Fig. 13 f, g) than over the bar. When waves propagate over the channel and break close to the shoreline, pressure gradient and $\partial S_{xx}/\partial x$ obtain greater values than at other alongshore positions (Fig.13h). The horizontal viscosity is always small except at locations with increased rip velocities, thus increasing the mixing within the rip channels. All these results were found to be qualitatively similar and in agreement with the experimentally-derived results of Haller et al. (2002).

4. Discussion

Overall results presented here indicate that the modifications introduced using the M08 formulation modified with a vertical distribution function as shown in Eqn. 10 ($M08_{vrt}$) provide results consistent with previous solutions in the depth-averaged sense, but also improve the

SUBMITTED

vertical distribution of the circulation patterns. In this section, our findings are explored for a more comprehensive discussion of the forces operating in the cases suitable for rip current development and in particular we discuss the implication for sediment transport and also the variability of rip current strength as function of the wave incident angle.

4.1. Cell circulation and potential morphological impacts.

Our Case 2 has re-affirmed how small differences in offshore wave height distribution can lead to the development of rip-current circulation patterns. However, one of the fundamental questions is the association of rip currents with bathymetry (i.e., bar-channel morphology). One suggestion from this work is that although a rip current circulation may develop due to offshore variable wave conditions, a positive feedback with the sea bed through sediment transport might lead to the bar-channel configuration that is usually associated with rip currents. In a simplified approach, we use results from Case 2 to assess the sediment transport patterns that such rip cells may create. Assuming that the combined action of wave oscillatory motion and mean current is the main mechanism for sediment resuspension and that the mean current is the advective transport mechanism (i.e., ignoring the effects of wave asymmetry) a simplified proxy for sediment erosion or accumulation can be established:

$$P_{ST} = \frac{\partial\left(U_t^2 \cdot \overline{u}\right)}{\partial x} + \frac{\partial\left(V_t^2 \cdot \overline{v}\right)}{\partial y} \qquad [16]$$

where, U_t is the total instantaneous maximum velocity, comprising of the vector sum of the wave orbital velocity and mean current vector and u and v are the cross-shore and alongshore Eulerian velocities, while the overbar denotes mean values. Although this proxy is very simplified and does not account for settling of sediment and other processes important in morphological evolution (see Warner et al., 2008), it gives some indication of the trend for bed

SUBMITTED

evolution under these conditions. As shown in Fig 14, the erosion potential is maximum at alongshore location λy=π, which corresponds to the area influenced by the outgoing rip current. The erosion potential reduces as we move towards the side boundaries λy=0 and λy=2π. Such tendency suggests that alongshore changes in wave forcing creating a rip current cell eventually might contribute to the development of the typical bar channel configuration.

4.2 Driving forces for Rip cell circulation

As described earlier, rip cells can be developed either due to alongshore variability in the offshore forcing of wave height (Case 2) or due to variability in the nearshore bathymetry (Case 3). In this section we attempt to examine the differences in the forces that drive the cell through an analysis of the depth and time averaged alongshore momentum balance (steady state, U and V are depth averaged Lagrangian velocities):

$$\frac{\partial}{\partial x}(U\cdot V\cdot h)+\frac{\partial}{\partial y}\left(V^2\cdot h\right)=-gh\frac{\partial \eta}{\partial y}-\frac{1}{\rho}\left(\frac{\partial S_{yy}}{\partial y}+\frac{\partial S_{xy}}{\partial x}\right)-\frac{\partial}{\partial y}\left(A_H\frac{\partial v}{\partial y}\right)-\frac{\tau_y^b}{\rho} \quad [17]$$

These terms are plotted in Fig. 15 as function of alongshore distance (normalized by the length scale of the offshore forcing (Case 2) or bathymetric perturbation as in Cases 3 and 4). The transects were taken well within the surf zone ensuring uniform alongshore water depth for Case 4 (Fig. 9, alongshore transect inshore of rip channel), and are located at the middle of the surf zone for Cases 2 and 3 (see dotted line in Figs. 3 and 7b respectively). The transect location for each case corresponds qualitatively to where the alongshore flows of the circulation cell (Fig 15a) converge to feed the main rip current. Case 2 produces an alongshore variability of the alongshore current that resembles the alongshore variability of the wave forcing, but being 90° out of phase. A similar alongshore variability is observed for Case 3 and 4, although in these

SUBMITTED

cases the peak alongshore feeder current is stronger than in Case 2 and located closed to the center of the rip cell.

The pressure gradient term (PG) shown in Figs 15b, c and d co-oscillates with the feeder current for each case. This indicates that pressure gradient is the dominant driver for both cases. However, within each case, the other terms exhibit similar relative behavior with the exception of the radiation stress (RAD_H) term that changes sign for each case. In Case 2 (Fig 15b) RAD_H is positive to the left of the rip channel and negative to the right, while the opposite is true for Cases 3 and 4 (see Fig. 15c & d). Also it is noticeable that the absolute values of the terms for Case 2 and Cases 3, 4 are almost an order of magnitude different, while the resulting absolute current velocities are of the same order. This increase in magnitude between the terms is attributed to the fact that in Case 3 and 4, the undulated bathymetry creates local wave refraction effects that lead to increased values of the S_{xy} term. This term qualitatively should be directed away from the center of the channel (location of minimum value) attaining a maximum value near the bathymetric highs. In terms of gradient, this corresponds to zero values at the center and either side of the channel as it appears to be the case in Fig 15c & d (zero values at 0.3, 0.5 and 0.7, respectively). In Case 2, the radiation stress gradient term is solely due to S_{yy} and it has a small value. This increased importance of radiation stress gradient in Cases 3 and 4 is compensated by an increase in the absolute value of the pressure gradient. The latter is driven partially by increased wave setup over the shoals due to bathymetry, but also due to increased wave height caused by focusing of the waves over the shoal due to refraction (i.e., the same process that increases the importance of the radiation stress gradient term). Thus overall, independent of the conditions (i.e., variable forcing or bathymetry), alongshore pressure gradient appears to be the main mechanism for the generation of feeder currents. Any increase in the

SUBMITTED

alongshore radiation stress term is compensated by similar increase in pressure gradient so that the net forcing remains of the same order. In all the cases discussed above, the horizontal advection contribution is dominant only within the rip channel area. Of the terms $\partial(V.V.h)/\partial y$ and $\partial(U.V.h)/\partial x$ responsible for horizontal advection, the latter has a greater magnitude in the vicinity of the rip channel because of stronger cross-shore velocity within the channel area.

4.3 Obliquely Incident Waves on LBT

In order to assess the effect of wave incidence angle to the development of rip current circulation a longshore bar-trough morphology domain as in Case 4 was subjected to offshore waves with height of 0.5 m and period of 3.16s incident at angles 0°, 5°, 10° and 20° with respect to the shore normal. The model uses two way coupling, allowing for interaction of waves and currents and the results are shown in Fig 16.

The top panel (Fig. 16) shows the depth averaged Eulerian velocity field in the rip channel for obliquely incident waves. As the incidence angle increases from 0° to 20°, the angle of exit of the rip current increase with respect to the shore normal. The trend is linear and for angles greater than 20° the current becomes almost parallel to the shoreline. Svendsen et al. (2000) simulated rip currents on barred beaches incised by channels using SHORECIRC and observed similar behavior of strong inertia of alongshore flow and weak rip currents for high wave angle of incidence. As expected the strength of alongshore velocity increases as the wave angle of incidence increases.

The wave height distribution over the domain, for different wave incidence angles, is shown in the middle panel of Fig. 16. When waves are normally incident, the rip current flow makes the waves steeper at the location of the channel, locally increasing the wave height (Fig.

SUBMITTED

16 column (a)). For incidence of 5°, wave steepening at the rip channel is also observed, but the increase in wave height is smaller than that observed for 0°. At higher angle of incidence (10°), wave current interaction reduces as only the component of the rip current along the direction of wave propagation interacts directly with the incoming waves. For waves coming at an angle of 20° to shore normal, the difference in wave breaking location over the bar and the channel is negligible further hinting at the lack of substantial rip currents.

Circulation pattern at the channel location is depicted through the vorticity vector (Fig. 16, bottom panel). For normal incidence primary and secondary circulation cell formation occurs outside the rip channel and close to the shoreline, respectively. These cells are symmetric about the rip channel center with opposite sign of vorticity indicating reverse sense of circulation. Such vortices are similar to the macrovortices formed due to wave breaking examined both analytically and computationally in Brocchini et al. (2004) and Kennedy et al. (2006). When waves are incident at 5°, the secondary circulation pattern weakens but the primary circulation pattern is reinforced as seen by increase in the magnitude of vorticity vector. Stretching and alongshore advection of vortices is also observed in this case. At a wave incidence of 10°, the secondary circulation cell close to the shoreline disappears and the vortices close to the channel become weak. The vorticity at the channel for 20° incidence shows only one circulation cell which is constrained at the original location where primary circulation was observed.

Fig. 17 (top panel) shows the Eulerian cross-shore velocity for varying angle of incidences (0°, 5°, 10°, 20°) in three columns (a), (b) and (c) corresponding to alongshore transects onshore and within the rip channel (see Fig. 16a top panel, alongshore transects). Rip current velocity at these locations is stronger when wave incidence is at 5° and 10°. Onshore of the channel, maximum offshore directed flow within the channel area occurs for 5° whereas at

SUBMITTED

transects within the channel, rip current velocity is slightly higher for 10° in comparison to 5° incidence (Fig. 17, top panel, column c). Higher angle of incidence (> 20°) inhibits rip currents due to inertia of alongshore motion. Aagaard et al. (1997) observed similar increase in the rip current velocity due to oblique incidence and attributed this phenomenon to "*wind enhanced longshore current*". Haller et al. (2002) observed an abrupt increase in cross-shore velocity for wave incidence angle of 10° in their test F. The reason for this behavior is suggested to be due to increase in alongshore radiation stress forcing in alongshore direction created by breaking of obliquely incident waves at the bar crest.

The contribution of alongshore velocity on rip current circulation pattern is determined by correlating the gradient of Eulerian alongshore velocity in alongshore direction (GAV) to the rip current magnitude. A steep gradient of alongshore velocity from one end of channel to other signifies a sharp change in alongshore velocity. The reduction of alongshore velocity feeds the alongshore momentum in cross-shore direction which intensifies the cross-shore velocity. Fig. 17 (bottom panel) shows GAV in alongshore direction for 0°, 5°, 10° and 20° angle of incidence for all three transects. The GAV values for 0° and 5° incidence show similar distribution pointing at presence of a circulation pattern whereas GAV distribution for 10° and 20° incidence are different implicating a loss of the circulation cells.

GAV is maximum for 5° at all locations except at the alongshore transect at center of the rip channel, where this quantity is equally steep for 10° (Fig. 17, bottom panel, column c). Thus most of alongshore momentum for 5° incidence advects through the rip channel due to the inherent rip current circulation in the domain. At higher angle of incidence the circulation pattern is destroyed and momentum transfer in cross-shore direction reduces. This information of

SUBMITTED

maximum rip current velocity for oblique incidence is useful for prediction of rip currents when waves coming at a small angle maybe more hazardous.

5. Conclusions

A full 3D, finite difference, circulation model Regional Ocean Modeling System (ROMS) coupled with spectral, phase averaged, wave propagation model SWAN has been updated to the formulations presented by Mellor (2008) and used to study nearshore circulation processes. The focus here was complicated flow regimes, including alongshore variability in wave height and water depth, i.e. phenomenon responsible for rip current like structure formation in the surf zone.

The results indicate that the implementation of the updated radiation stress forcing with a modified vertical distribution ($M08_{vrt}$) that incorporates wave height as a scale significantly improves the performance of the model creating vertical profiles of cross-shore velocities that are both realistic and in agreement with experimental results.

Comparisons of the depth integrated circulation of the 3-D runs were found to be in agreement with the general dynamics for formation of nearshore circulation cell on normal incidence of alongshore varying wave height over a planar bathymetry (Bowen, 1969) and under alongshore variable bathymetry forced with alongshore uniform wave height (Noda, 1974). Furthermore, it has been shown that increasing the Reynolds number by decreasing the viscosity, the circulation cells become skewed with the offshore directed flow becoming narrower and faster while onshore flow broadens and becomes slower. The development of the model provided us with insights on the vertical distribution of the cross-shore velocities in these

SUBMITTED

circulation patterns allowing us to provide an insight into wave breaking induced flow at the surface and bottom boundary layer.

The new formulation of radiations stress forcing demonstrated a strong agreement with the scaled up laboratory experiments of Haller et al. (2002) and Haas and Svendsen (2002).

By using a proxy for sediment transport, it is determined that rip current circulation cells formed due to differences in alongshore wave forcing may lead to formation of alongshore barred beaches interrupted by rip channels.

Finally, the effect of obliquely incident waves on rip channels is studied and it is found that rip current strength observed within the channel is stronger when waves come at angle of 5° and 10° in comparison to normally incident waves. This information may be helpful in prediction of rip currents.

Overall the implementation of Mellor (2008) based distribution of vertical radiation stress along with a vertical scaling as a function wave height ($M08_{vrt}$) improves the ability of coupled ROMS-SWAN model in resolving wave and current effects in the surf zone. This modeling tool can be used to understand the physical mechanism for phenomenon observed in surf zone along with prediction of nearshore circulation.

Acknowledgements

Funding for this study has been obtained by a number of sources. The first two authors were supported by a NOAA/IOOS Grant (Integration of Coastal Observations and Assets in the Carolinas in Support of Regional Coastal Ocean Observation System Development in the Southeast Atlantic) and a cooperative agreement between U.S. Geological Survey, and University of South Carolina as part of the Carolinas Coastal Change Processes Project. Also G.

SUBMITTED

Voulgaris was partially supported by the National Science Foundation (Awards: OCE-0451989 and OCE-0535893). The authors thank the two anonymous reviewers for their comments and suggestions on the manuscript. Finally, we would also like to thank the ROMS and SWAN code developers for their hard work in developing this open source code.

SUBMITTED

Appendix A

Mellor (2003) introduced depth dependent formalism for radiation stresses to accommodate wave averaged effects on mean currents. These formulations when vertically integrated are consistent with the depth integrated solution of Longuet-Higgins and Stewart (1964). Ardhuin et al. (2008) showed that use of the M03 formulation in non breaking wave propagation over an uneven topography produces a spurious circulation pattern at the location where $\partial h/\partial x \neq 0$. In response to this, a new set of depth dependent equations for wave current interaction was presented (Mellor, 2008), which has been further modified and implemented in this paper for applications in the surf zone. Mellor (2008, see Section 2) suggested that for variable topography, the new set of equations would cause some errors but overall there is a good chance that these equations can be applied to shallow water environment (i.e., $kD \approx 1$, where k is the wave number and D is the total water depth), when effects of viscosity and turbulence are included. In this section we test the above argument by carrying out two numerical simulations corresponding to the setup originally proposed by Ardhuin et al. (2008) and to a setup using a milder slope that is found in Duck, NC and including friction and mixing processes. Both setups are forced with a shoaling, non-breaking monochromatic wave with a significant wave height of 1.02 m and wave period . of 5.24 s, propagating from east to west. These runs are described in some detail below.

In the setup resembling Ardhuin's et al. (2008) conditions the bottom profile has a channel in which the water depth smoothly transitions from 6 m to 4 m (dh/dx_{max}= 0.0266), and is symmetric about the vertical axis at the center (i.e., x= 300 m, Fig. A1a). The non dimensional water depth, kD varies from $0.85 < kD < 1$ (Fig. A1b). The model domain is alongshore uniform with a cross-shore width (x) of 600 m and an alongshore length (y) of 800 m. Grid resolution is 4

SUBMITTED

m and 100 m in x and y direction, respectively. The vertical domain has been distributed in 32 vertical layers. The boundary conditions are constant flux at east and west boundary (Neumann conditions) and closed in the north and south. Effect of earth's rotation, bottom stress and viscosity have not been included in this case. Simulations have been done using both $M08_{top}$ and $M08_{vrt}$ formulations.

In absence of wave breaking, mixing and bottom friction the only dynamic effects occur due to changes in wave height. Shoaling of waves in shallower waters create divergence of the Stokes drift which is compensated by the Eulerian mean current. The correct representation of Lagrangian velocity field (Eulerian + Stokes) for this wave field and domain setup is a flow along the direction of wave propagation ($U_l = 0.025$ ms^{-1}) at the surface which decreases gradually to no flow at z= -2 m and then changes to a return flow of $U_l = -0.01$ ms^{-1} close to bottom layer. The flow field at the surface and bottom follows the bathymetric contours (see Fig. 2, in Bennis and Ardhuin, submitted, http://arxiv.org/PS_ cache/arxiv/pdf/1003/1003.0508v1.pdf).

The vertical profile of Lagrangian cross-shore velocity based on $M08_{top}$ are shown in Figs. A2a. At the location where $dh/dx \neq 0$ and where the waves are propagating upslope, spurious flow pattern is observed in the upper half of the water column showing a current along the direction of wave propagation (U_{lmax}=0.15 ms^{-1}) and a compensating flow, of same strength but opposite sign, in the lower half of the water column. A reversed flow structure is established on the down-slope wave propagation region (Fig. A2a). When we use $M08_{vrt}$ based formulations (Fig. A2b), significant part of the water column shows a weak flow, $U_l \approx$ 0.01-0.10 ms^{-1} towards wave propagation direction, while the surface layer shows a relatively stronger flow of 0.20-0.25 ms^{-1} in opposite direction. The flow field is reversed when waves propagate down the slope.

SUBMITTED

Irrespective of updating the formulation for radiation stresses, in an idealistic situation, M08 and $M08_{vrt}$ based simulation still create incorrect flow patterns for unforced waves traversing on a sloping bottom. This is consistent with Bennis and Ardhuin (submitted) and Ardhuin et al. (2008).

The second setup uses a milder, more realistic slope dh/dx_{max}= 0.0066, bottom friction (quadratic drag, C_d=0.003) and mixing (constant eddy viscosity, 0.0028 m^2s^{-1}). The domain is also symmetric about the vertical axis at the center (i.e., x= 1200 m, Fig. A1c). The non dimensional water depth, *kD* is the same as before. The model domain is alongshore uniform with a cross-shore width (x) of 2400 m and an alongshore length (y) of 800 m. Grid resolution and vertical domain remain the same as previously. In this run the Lagrangian velocity (Fig A2c) is along the direction of wave propagation at the surface layer except at the upslope wave propagation location where small perturbations in the velocity flow field are observed.. Compensating return flow in the lower half of water column is also observed. However, the strength of Lagrangian velocity is reduced by a factor of ~5 when compared to the ideal conditions (Fig. A2a and b). Also it is noticeable that velocity contours "try" to follow the bathymetric contours as in Bennis and Ardhuin (submitted).

The maximum velocity at the surface in Fig. A2c is twice the velocity calculated by Bennis and Ardhuin (submitted), hence the flow field may be still slightly erroneous. Bennis and Ardhuin (submitted) also stated (but not shown) that on using a realistic mixing, the erroneous flow reduces by a factor of 4 from that estimated for a higher bottom slope (Fig. A1a). In addition, all the simulations presented in this contribution (Cases 1-4) are for surf zone conditions, where the wave breaking induced flow is an order of magnitude higher than the topography-induced flow shown in Fig. A2c (i.e., realistic topography and mixing). This

SUBMITTED

suggests that although the Mellor (2008) formulation is mathematically inconsistent the errors might be inconsequential for practical applications. This will be even more valid when injection of wave turbulence and wave roller processes are included which would further reduce the importance of these discrepancies in the mean flow.

SUBMITTED

References

Aagaard, T., Greenwood, B., Nielsen, J., 1997. Mean currents and sediment transport in a rip Channel. Marine Geology 140, 25-45.

Ardhuin, F., Jenkins, A.D, Belibassakis, K.A., 2008a. Comments on “The three-dimensional current and surface wave equations”. J. Phys. Oceanogr. 38, 1340–1350.

Arthur, R. S. 1962. A Note on the Dynamics of Rip Currents. J. Geophys. Res. 67(7), 2777–2779.

Battjes, J.A., Janssen, J.P.F.M., 1978. Energy loss and set-up due to breaking of random waves. Proc. 16th Int. Conf. Coastal Engineering, ASCE, pp. 569-587.

Bennis, A., Ardhuin, F.,. On the vertical structure of the wave forcing for the ocean circulation (submitted, Journal of Physical Oceanography).

Booij, N., Ris, R. C., Holthuijsen, L. H., 1999. A third-generation wave model for coastal regions 1. Model description and validation, J. Geophys. Res. 104(C4), 7649–7666.

Bowen, A. J., 1969. Rip Currents 1. Theoretical Investigations. J. Geophys. Res. 74(23), 5467–5478.

Bowen, A. J., Inman D. L., 1969. Rip Currents 2. Laboratory and Field Observations. J. Geophys. Res. 74(23), 5479–5490.

Brander, R.W., Short A.D., 2001. Flow kinematics of low-energy rip current systems. J. Coastal Res. 17 (2), 468–481.

Brocchini, M., Kennedy, A. B., Soldini, L., Mancinelli, A., 2004. Topographically controlled, breaking-wave-induced macrovortices. Part 1. Widely separated breakwaters. J. Fluid Mech. 507, 289–307.

Chen, Q., Dalrymple, R. A., Kirby, J. T., Kennedy, A. B., Haller, M. C., 1999. Boussinesq

SUBMITTED

modeling of a rip current system. J. Geophys. Res. 104(C9), 20,617–20,637.

Church, J. C., Thornton, E.B., 1993. Effects of breaking wave induced turbulence within a longshore current model. Coastal Engineering 20, 1–28.

Craik, A.D.D., Leibovich, S., 1976. A rational model for Langmuir circulations. J. Fluid Mech. 73, 401-426.

Dalrymple, R. A., 1975. A Mechanism for Rip Current Generation on an Open Coast. J. Geophys. Res. 80(24), 3485–3487.

Drønen, N., Karunarathna, H., Fredsoe, J., Sumer, M., Deigaard, R., 2002. An experimental study of rip channel flow. Coastal Engineering. 45, 223-238.

Eldeberky, Y., Battjes, J. A., 1996. Spectral modeling of wave breaking: Application to Boussinesq equations. J. Geophys. Res. 101, 1253–1264.

Feddersen, F., Guza, R. T., Elgar, S., Herbers, T. H. C., 1998. Alongshore momentum balances in the nearshore. J. Geophys. Res. 103, 15,667–15,676

Garcez-Faria, A. F., Thornton, E. B., Lippmann, T. C., Stanton, T. P., 2000. Undertow over a barred beach. J. Geophys. Res. 105, 16,999–17,010.

Groeneweg, J., Klopman, G., 1998. Changes in the mean velocity profiles in the combined wave–current motion described in GLM formulation. J. Fluid Mech. 370, 271–296.

Haas, K. A., Svendsen, I. A., Zhao, Q., 2000. 3D modeling of rip currents. Proceedings 27th Coastal Engineering Conference, American Society Civil Engineers, Sydney, Australia, 2, pp. 1113-1126.

Haas, K. A., Svendsen, I. A., 2002. Laboratory measurements of the vertical structure of rip currents. J. Geophys. Res. 107(C5), 3047, doi: 10.1029/2001JC000911.

SUBMITTED

Haas, K. A., Svendsen, I. A., Haller, M. C., Zhao, Q., 2003. Quasi-three-dimensional modeling of rip current systems, J. Geophys. Res., 108(C7), 3217, doi: 10.1029/2002JC001355.

Haas, K. A., Warner, J.C., 2009. Comparing a quasi-3D to a full 3D nearshore circulation model: SHORECIRC and ROMS. Ocean Modeling. 26, 91–103.

Haidvogel, D. B. , Arango, H.G., Budgell, W. P., Cornuelle, B. D., Curchitser, E., Di Lorenzo, E., Fennel, K., Geyer, W. R., Hermann, A. J., Lanerolle, L., Levin, J., McWilliams, J. C., Miller, A. J., Moore, A. M., Powell, T. M., Shchepetkin, A. F., Sherwood, C. R., Signell, R. P., Warner, J. C., Wilkin, J., 2008. Regional Ocean Forecasting in Terrain-following Coordinates: Model Formulation and Skill Assessment, Journal of Computational Physics. 227, 3595-3624.

Haller, M. C., Dalrymple, R.A., Svendsen, I. A., 2002. Experimental study of nearshore dynamics on a barred beach with rip channels. J. Geophys. Res. 107(C6), 3061, doi:10.1029/2001JC000955.

Haller, M. C., Dalrymple, R. A., 2001. Rip current instabilities. Journal of Fluid Mechanics. 433, 161-192.

Hughes, S.A., 1993. Physical Models and Laboratory Techniques in Coastal Engineering. World Scientific, Singapore.

Huntley, D.A., Short, A.D., 1992. On the spacing between observed rip currents. Coastal Engineering. 17, 211–225.

Kennedy, A. B., Brocchini, M., Soldini, L., Gutierrez, E., 2006. Topographically controlled, breaking-wave-induced macrovortices. Part 2. Changing geometries. J. Fluid Mech. 559, 57–80.

LeBlond, P. H., Tang, C. L., 1974. On Energy Coupling Between Waves and Rip Currents. J. Geophys. Res. 79(6), 811–816.

Lesser, G.R., Roelvink, J.A., van Kester, J.A.T.M., Stelling, G.S., 2004. Development and

SUBMITTED

validation of a three-dimensional morphological model. Coastal Engineering. 51, 883-915.

Long, J. W., Özkan-Haller, H. T., 2009. Low-frequency characteristics of wave group–forced vortices. J. Geophys. Res. 114, C08004, doi: 10.1029/2008JC004894.

Longuet-Higgins, M.S. (1953), Mass Transport in Water Waves, Philosophical Transactions of the Royal Society of London, Series A 245: 535–581.doi: 10.1098/rsta.1953.0006.

Longuet-Higgins, M. S., Stewart, R.W., 1964. Radiation stresses in water waves: a physical discussion, with applications. Deep-Sea Res. 11, 529–562.

Longuet-Higgins, M. S., 1970. Longshore Currents Generated by Obliquely Incident Sea Waves. a, b, J. Geophys. Res. 75(33), 6778–6801.

MacMahan, J.H., Thornton, E. B., Stanton, T.P., Reniers, A.J.H.M, 2005. RIPEX: Observations of a rip current system. Marine Geology. 218 (1-4), 113-134, doi:10.1016/j.margeo.2005.03.019.

Madsen, O.S., Poon, Y.K., Graber, H.C., 1988. Spectral wave attenuation by bottom friction: Theory. Proc. 21th Int. Conf. Coastal Engineering, ASCE, pp. 492-504

McWilliams, J.C., Restrepo, J.M., Lane, E.M., 2004. An asymptotic theory for the interaction of waves and currents in coastal waters. Journal of Fluid Mechanics. 511, 135–178.

Mellor, G. L., 2003. The three-dimensional current and surface wave equations. J. Phys. Oceanogr. 33, 1978–1989.

Mellor, G. L., 2005. Some consequences of the three-dimensional currents and surface wave equations. J. Phys. Oceanogr. 35, 2291-2298.

Mellor, G. L., 2008. The depth-dependent current and wave interaction equations: A revision. J. Phys. Oceanogr. 38, 2587-2596.

Newberger, P. A., Allen, J. S., 2007. Forcing a three-dimensional, hydrostatic, primitive equation model for application in the surf zone: 1. Formulation, J. Geophys. Res. 112, C08018,

SUBMITTED

doi:10.1029/2006JC003472.

Noda, E. K., 1974. Wave-Induced Nearshore Circulation. J. Geophys. Res. 79(27), 4097–4106.

Reniers, A. J. H. M., Roelvink, J. A., Thornton, E. B., 2004a. Morphodynamic modeling of an embayed beach under wave group forcing. J. Geophys. Res. 109, C01030, doi:10.1029/2002JC001586.

Ruessink, B. G., Miles, J. R., Feddersen, F., Guza, R. T., Elgar, S., 2001. Modeling the alongshore current on barred beaches. J. Geophys. Res. 106(C10), 22,451–22,463.

Shchepetkin, A. F., McWilliams, J.C., 2005. The Regional Oceanic Modeling System: A split-explicit, free-surface, topography-following coordinate oceanic model. Ocean Modeling 9, 347–404 doi:10.1016/j.ocemod.2004.08.002.

Shchepetkin, A. F., McWilliams, J. C., 2009. Correction and commentary for "Ocean forecasting in terrain-following coordinates: Formulation and skill assessment of the regional ocean modeling system" by Haidvogel et al., J. Comp. Phys. 227, pp. 3595–3624.". Journal of Computational Physics. 228, 8985-9000.

Sonu, C. J., 1972. Field Observation of Nearshore Circulation and Meandering Currents. J. Geophys. Res. 77 (18), 3232–3247.

Stive, M. J. F., De Vriend, H.J., 1994. Shear stresses and mean flow in shoaling and breaking waves. Proc. of the 24th Coastal Engineering International Conference 1994, Kobe, Japan. American Society of Civil Engineers, New York, pp. 594–608.

Svendsen, I. A., Haas, K. A., Zhao, Q., 2000. Analysis of rip current systems. In Proceedings 27th Coastal Engineering Conference, ASCE, Sydney, pp. 1127-1140.

Svendsen, I.A., Haas, K.A., Zhao, Q., 2002. Quasi-3D nearshore circulation model

SUBMITTED

SHORECIRC, User's Manual, Draft Report, Center for Applied Coastal Research, Department of Civil Engineering, University of Delaware, Newark.

Tam, C. K. W., 1973. Dynamics of Rip Currents. J. Geophys. Res. 78(12), 1937–1943.

Terrile, E., Brocchini, M., 2007. A dissipative point-vortex model for nearshore circulation. J. Fluid Mech., 589, pp. 455-478.

Ting, F.C.K., Kirby, J.T., 1994. Observations of undertow and turbulence in a laboratory surf zone. Coastal Engineering. 24, 177-204.

Uchiyama, Y., McWilliams, J.C., Shchepetkin, A.F., 2010, Wave-current interaction in an Oceanic Circulation Model with a Vortex- Force Formalism: Application to the Surf Zone. Ocean Modeling, doi: 10.1016/j.ocemod.2010.04.002.

van Dongeren, A.R., Sancho, F.E., Svendsen, I.A., Putrevu, U., 1995. Application of the Q3d SHORECIRC model to surfbeat. Proc. Coastal Dynamics, Gdynia, Poland, ASCE, New York, pp. 233–244.

Walstra, D. J. R., Roelvink, J.A., Groeneweg, J., 2000. Calculation of wave-driven currents in a 3D mean flow model. Proc. of the 27th Coastal Engineering International Conference 2000, Sydney, Australia. American Society of Civil Engineers, New York, pp. 1050–1063.

Warner, J.C., Sherwood, C.R., Arango, H.G., Signell, R.P., Butman, B., 2005. Performance of four turbulence closure models implemented using a generic length scale method. Ocean Modeling. 8, 81–113.

Warner, J.C., Sherwood, C.R., Signell, R.P., Harris, C., and Arango, H.G., 2008. Development of a three-dimensional, regional, coupled wave, current, and sediment-transport model. Computers and Geosciences. 34, 1284-1306.

Yu, J., Slinn, D. N., 2003. Effects of wave-current interaction on rip currents. J. Geophys.

SUBMITTED

Res. 108(C3), 3088, doi:10.1029/2001JC001105.

SUBMITTED

Figure Captions

Figure 1. Case 1: Obliquely incident waves on a planar beach using the original radiation stress forcing M03, the updated forcing applied at the top layer $M03_{top}$, and with a vertical distribution as defined by Eq. 10 of $M08_{vrt}$. Cross-shore distribution of: (a) significant wave height (m), water depth (m) and sea surface elevation (m); The water depth and wave height have been scaled as h/20 and $H_{sig}/10$ respectively; (b) depth averaged Eulerian cross-shore velocity ($\bar{u}$); and (c) depth averaged Eulerian alongshore velocity ($\bar{v}$).

Figure 2. Comparison of vertical profile of cross-shore Eulerian velocity, u(x, z) between simulations using M03 (solid grey line), $M08_{top}$ (dashed black line), $M08_{vrt}$ (solid black line). The sea surface elevation (ζ, dotted grey line) is also shown. Vertical black lines indicate locations of model sampling and zero value for each profile.

Figure 3. Color shading of significant wave height distribution over the computational domain after 2 hours of model simulation for two way coupling between ROMS and SWAN. Note the significant wave height at offshore boundary is 1.5 m at the ends and decreases to a minimum value of 1m at the center of the domain. The alongshore and cross-shore domain has been scaled by a value of ($\lambda=2\pi/1000$). Dashed lines indicate the location of transects shown in Figure 6 and dotted lines indicate the location of alongshore transect shown in Figure 15.

Figure 4. Rip current simulation results for the bottom half of the computational domain (Case 2, two-way coupling) after 2 hours of simulation. (a) Depth averaged Lagrangian velocity

SUBMITTED

distribution; (b) Transport stream function (ψ) showing formation of circulation cell in the surf zone; (c) Transport stream function (ψ) calculated using the analytical solution provided by Bowen, 1969 for the present model setup. Note: $\lambda x=\pi/2$ is the location where waves start breaking.

Figure 5. Transport stream function, ψ over the computational domain for Reynolds Number (Re) values of (a) 500, (b) 125, (c) 62.5, and (d) 42. Note the solution gets skewed about the individual centers of the circulation cells with increased Re value causing a narrower outflow from shallow to deeper waters and broader inflow from deeper to shallower waters. Also note that the individual circulation cells are not exactly symmetric about the line $y= \pi$. The grey circulation cell in (a), (b), and (c) is same as (d); it is shown for comparison purposes.

Figure 6. Contour plots showing the vertical structure of the Eulerian cross-shore (a, b, c) and alongshore velocity (d, e, f) along three transects located at $\lambda y=\pi/5$ (a, d), $\lambda y=\pi/2$ (b, e), and $\lambda y=4\pi/5$ (c, f) from the southern lateral boundary (see dashed lines in Figure 3). Solid black line corresponds to zero velocity.

Figure 7. (a) Depth averaged Eulerian velocity (black arrows) after 1 hour of simulation. Light grey lines in background depict the bathymetry contours; (b) Contour of significant wave height distribution over the computational domain. The incident wave height at the offshore boundary of the domain is 0.92 m. Contour plots showing the vertical structure of cross-shore Eulerian velocity, u(x, z) along two transects located at (c) y=0 m, (d) y=40 m from the southern lateral

SUBMITTED

boundary (see grey lines in Figure 7b). The grey dotted alongshore transect in Fig. 7b is location at which alongshore momentum balance term is shown in Fig. 15(c).

Figure 8. Transport stream function (ψ) over the computational domain computed from the model results after (a) depth averaging the horizontal Lagrangian velocity field; (b) and from Noda (1974) paper.

Figure 9. Bathymetry for Case 4, showing the longshore bar and the rip channels. The solid black lines show the location of vertical transects at which the cross-shore velocity distribution is discussed in Fig. 12. The 4 horizontal white lines represent the alongshore transects at which cross-shore momentum balance terms are shown in Fig. 13 and alongshore momentum balance term is shown in Fig. 15(d).

Figure 10. Contours of significant wave height after 30 minutes of model simulation using (a) the original version of the model as in HW09 and; (b) the updated model with the M08 formulations for the vertical distribution of the radiation stress ($M08_{vrt}$). Bathymetric contours and depth integrated Eulerian mean currents over the computational domain using (c) the original version of the model as in HW09 and; (d) the updated model with the M08 formulations for the vertical distribution of the radiation stress ($M08_{vrt}$). The black line (10c) depicts a velocity of 0.5 ms^{-1}.

Figure 11. Cross-shore variation of mean sea surface elevation at two locations corresponding to alongshore positions centered at the middle of the rip channel (black) and alongshore bar (grey).

SUBMITTED

Figure 12. Vertical structure of cross-shore Eulerian velocity u(x,z) at the center of rip channel (a and b) and bar (c and d) derived from original version of the model as in HW09 (a and c) and the updated model with the M08 formulations($M08_{vrt}$) (b and d); (e) Comparison of normalized model derived cross-shore velocity with normalized data from Haas and Svendsen, 2002 (key: symbols ● and ■ denote data at the center and 4m off the channel, grey line (center of the channel M03), black dash dot (center of the channel $M08_{vrt}$), blue dashed line ($M08_{vrt}$, 4 m off the channel)).

Figure 13. Alongshore variation of the depth averaged cross-shore momentum balance equation terms. Horizontal advection (ADV_H, $\partial/\partial x(U^2h)+\partial/\partial y(UVh)$, black line), bottom stress (BT, τ_x/ρ, grey line) and radiation stress forcing ($\partial S_{xy}/\rho\partial y$, black dashed) terms are shown in (a) to (d). Cross-shore pressure gradient (PG, $gh(\partial\eta/\partial x)$, black line), radiation stress forcing (RAD_H, $\partial S_{xx}/\rho\partial x$, grey line) and horizontal viscosity ($VISC_H$, $\partial(A_H\partial u/\partial x)/(\rho\partial x)$), black dashed) are shown in (e) to (h). The distances at which the terms are estimated are 40 m (a) and (e), 30 m (b) and (f), 26 m (c) and (g), and 20 m (d) and (h) from the shoreline (see Fig. 9).

Figure 14. Contour of sediment transport proxy (P_{st}) over computational domain for the run of Case 2 of alongshore variable wave forcing.

Figure 15. (a) Depth averaged alongshore Eulerian velocity, V (ms^{-1}) at alongshore transects shown by dotted line in Fig.3 for Case 2, dotted line in Fig.7b for Case 3 and alongshore transect onshore of the rip channel (Fig. 9) for Case 4; Alongshore variation of the depth averaged

SUBMITTED

alongshore momentum balance terms for (b) Case 2 and (c) Case 3 for alongshore transect as 15(a), (d) Case 4 for alongshore transect as 15(a). The alongshore normalizing length scale (L_y) used in (b), (c) and (d) are 1000 m, 80 m and 90 m, respectively, and represent the corresponding perturbation length in forcing or bathymetry (key: alongshore pressure gradient (PG, $gh(\partial\eta/\partial y)$, black line), radiation stress forcing (RAD_H, $(\partial S_{yy}/(\rho\partial y)+\partial S_{xy}/(\rho\partial x))$, black dashed), Horizontal advection (ADV_H, $\partial/\partial x(UVh)+\partial/\partial y(V^2h)$, grey line), bottom stress (BT, τ_y/ρ, grey dashed-dot line))

Figure 16. Circulation (depth averaged, Eulerian current vector, top row), significant wave height distribution (middle row) and vorticity field (bottom row) results for different wave incident angles (columns a to d, corresponding to incident angles of 0, 5, 10 and 20 degrees, respectively) The thin grey lines in top row, column (a) show the alongshore transects at which relevant terms are plotted in Figure. 17. Note: The bathymetry used in this case is same as Figure 9, but only the relevant part of the domain has been shown here.

Figure 17. Eulerian cross-shore velocities (top panel) and absolute value of alongshore gradient of Eulerian alongshore velocities (bottom panel) at 3 alongshore transects located (a) 16 m (b) 22 m (c) 28 m from the shoreline as shown by grey lines n Fig. 16 (top panel, column (a)) for waves incident at angles 0^o, 5^o, 10^o, 20^o .

Figure A1. Model forcing (wave height) and non dimensional depth (a and c) and bottom bathymetry (b and d) used to test the Mellor (2008) formulation. (a) and (b) are identical as in

SUBMITTED

Ardhuin et al. (2008). Forcing in (c) is the same as (a) but the bathymetry (d) has a reduced bottom slope (note differences in horizontal scale between b and d).

Figure A2. Vertical distribution of Lagrangian velocity, U_l (Eulerian velocity + Stokes drift) calculated using (a) $M08_{top}$ with a domain geometry as in Ardhuin et al. (2008); (b) $M08_{vrt}$ on the same domain as (a); and (c) $M08_{vrt}$ with a similar geometry but reduced bottom slope (note differences in horizontal scale), uniform vertical mixing and bottom friction. Contour line spacing is 0.01 ms^{-1} in (a), (b) and 0.002 ms^{-1} in (c). Note different scales in colorbar used in (c).

SUBMITTED

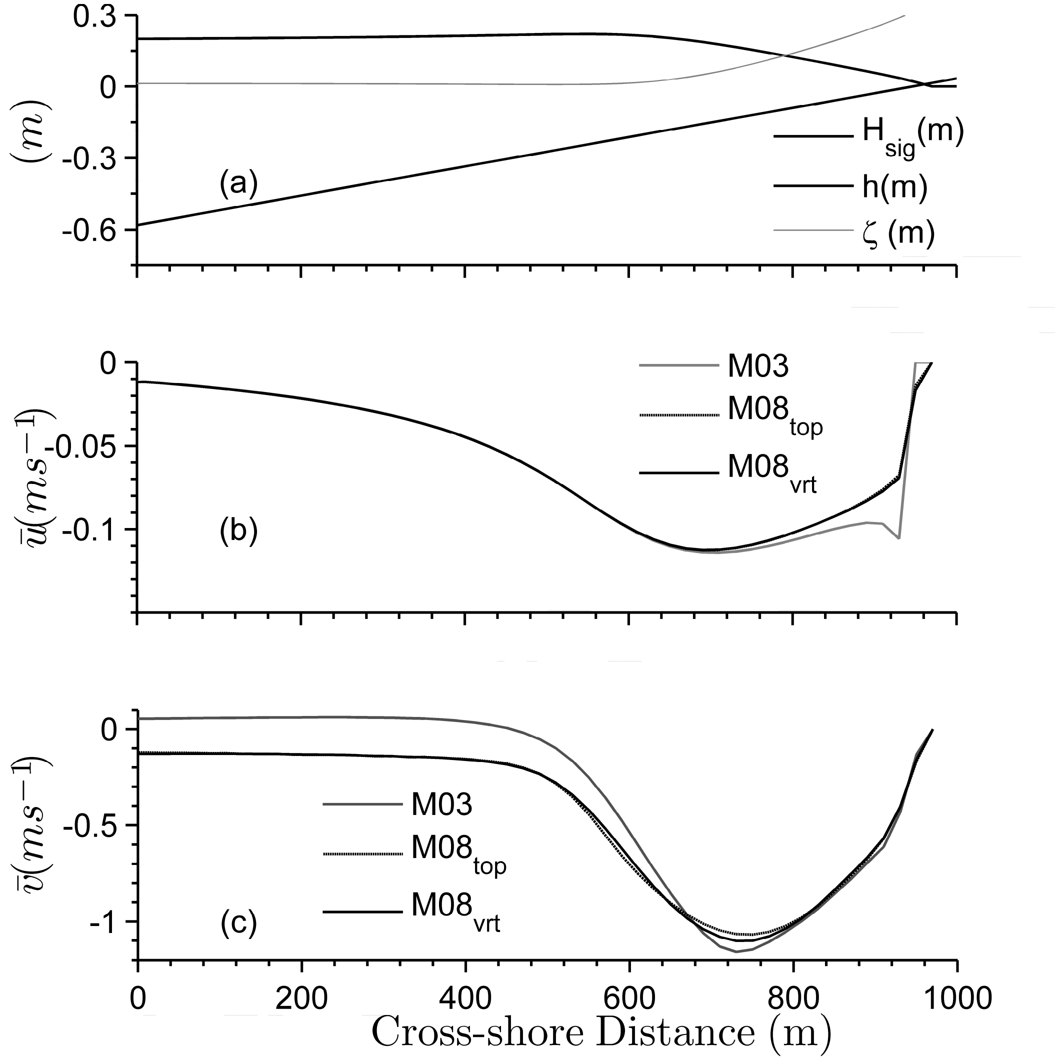

Figure 1. Case 1: Obliquely incident waves on a planar beach using the original radiation stress forcing M03, the updated forcing applied at the top layer $M03_{top}$, and with a vertical distribution as defined by Eq. 10 of $M08_{vrt}$. Cross-shore distribution of: (a) significant wave height (m), water depth (m) and sea surface elevation (m); The water depth and wave height have been scaled as h/20 and $H_{sig}/10$ respectively; (b) depth averaged Eulerian cross-shore velocity ($\bar{u}$); and (c) depth averaged Eulerian alongshore velocity ($\bar{v}$).

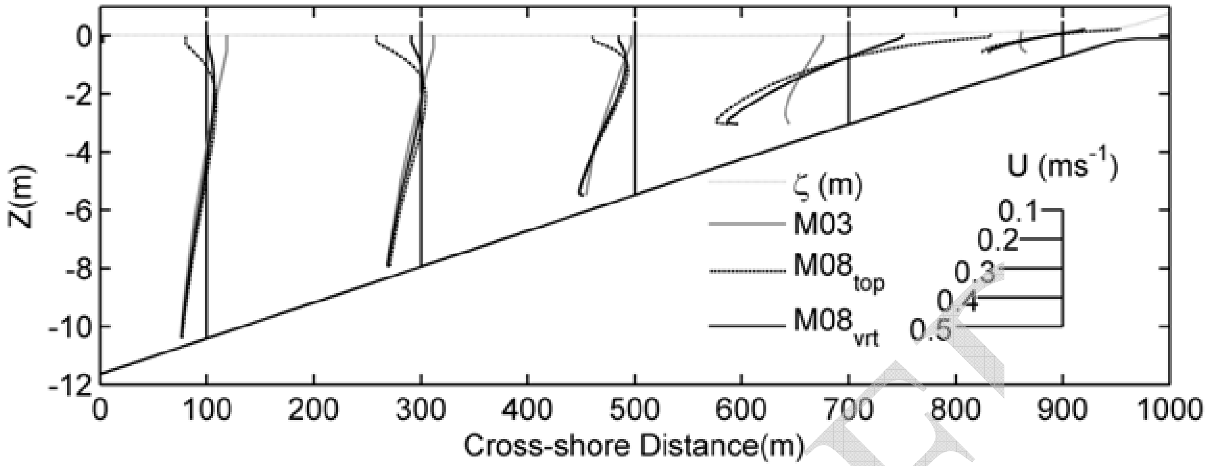

Figure 2. Comparison of vertical profile of Eulerian cross-shore velocity, u(x, z) between simulations using M03 (solid grey line), $M08_{top}$ (dashed black line), $M08_{vrt}$ (solid black line). The sea surface elevation (ζ, dotted grey line) is also shown. Vertical black lines indicate locations of model sampling and zero value for each profile.

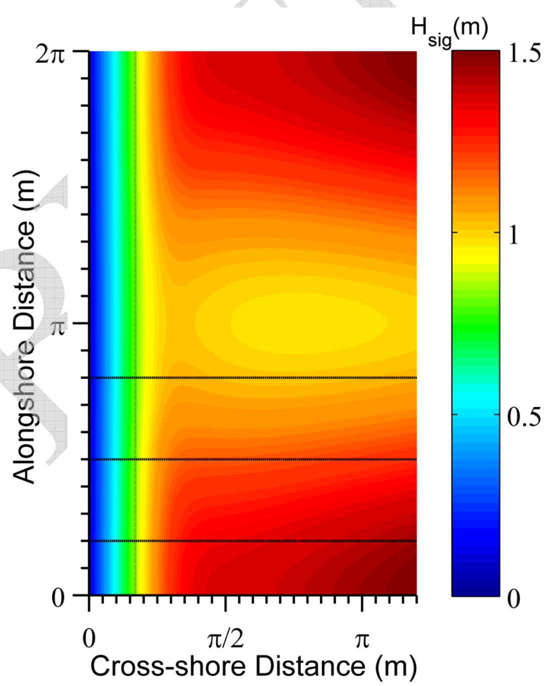

Figure 3. Color shading of significant wave height distribution over the computational domain after 2 hours of model simulation for two way coupling between ROMS and SWAN. Note the significant wave height at offshore boundary is 1.5 m at the ends and decreases to a minimum value of 1m at the center of the domain. The alongshore and cross-shore domain has been scaled by a value of (λ=2π/1000). Dashed lines indicate the location of transects shown in Figure 6 and dotted lines indicate the location of alongshore transect shown in Figure 15.

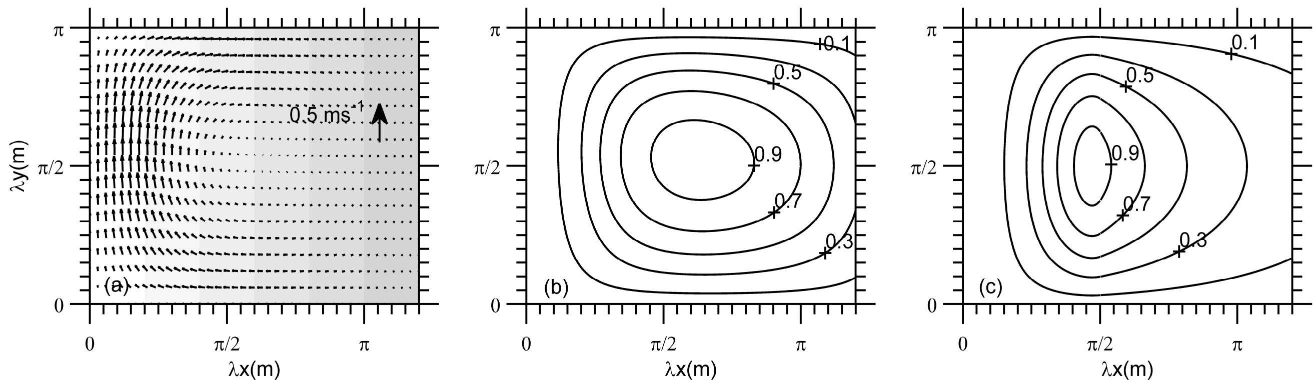

Figure 4. Rip current simulation results for the bottom half of the computational domain (Case 2, two-way coupling) after 2 hours of simulation. (a) Depth averaged Lagrangian velocity distribution; (b) Transport stream function (ψ) showing formation of circulation cell in the surf zone; (c) Transport stream function (ψ) calculated using the analytical solution provided by Bowen, 1969 for the present model setup. Note: λx=π/2 is the location where waves start breaking.

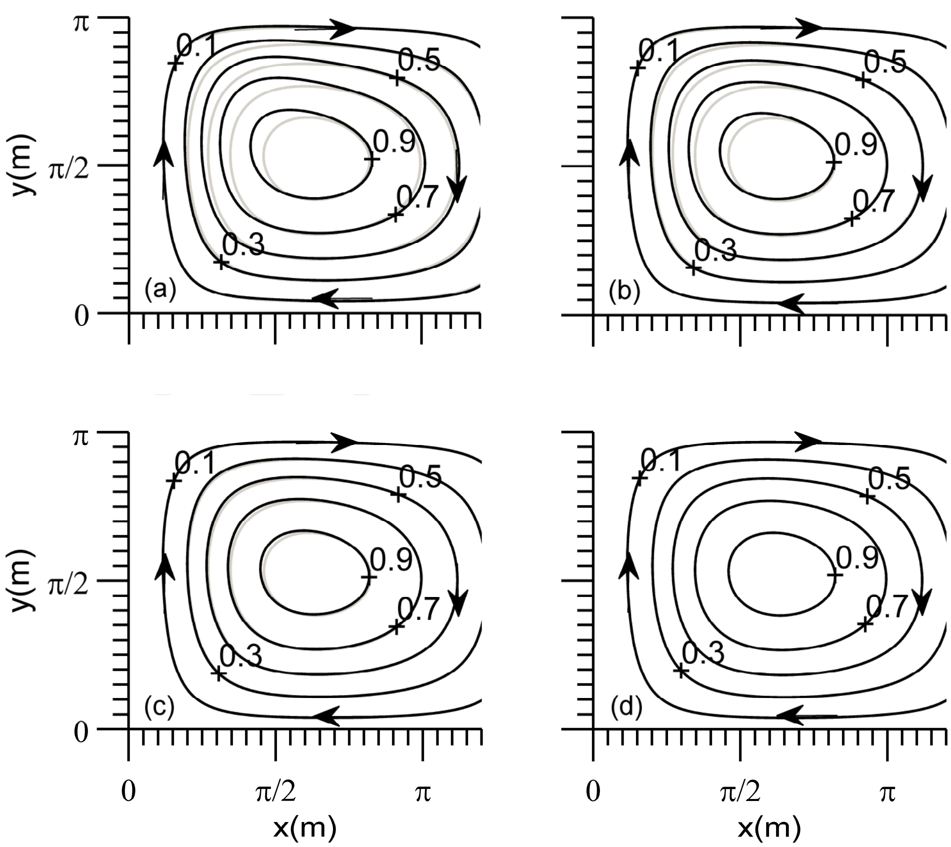

Figure 5. Transport stream function, ψ over the computational domain for Reynolds Number (Re) values of (a) 500, (b) 125, (c) 62.5, and (d) 42. Note the solution gets skewed about the individual centers of the circulation cells with increased Re value causing a narrower outflow

from shallow to deeper waters and broader inflow from deeper to shallower waters. Also note that the individual circulation cells are not exactly symmetric about the line y= π. The grey circulation cell in (a), (b), and (c) is same as (d); it is shown for comparison purposes.

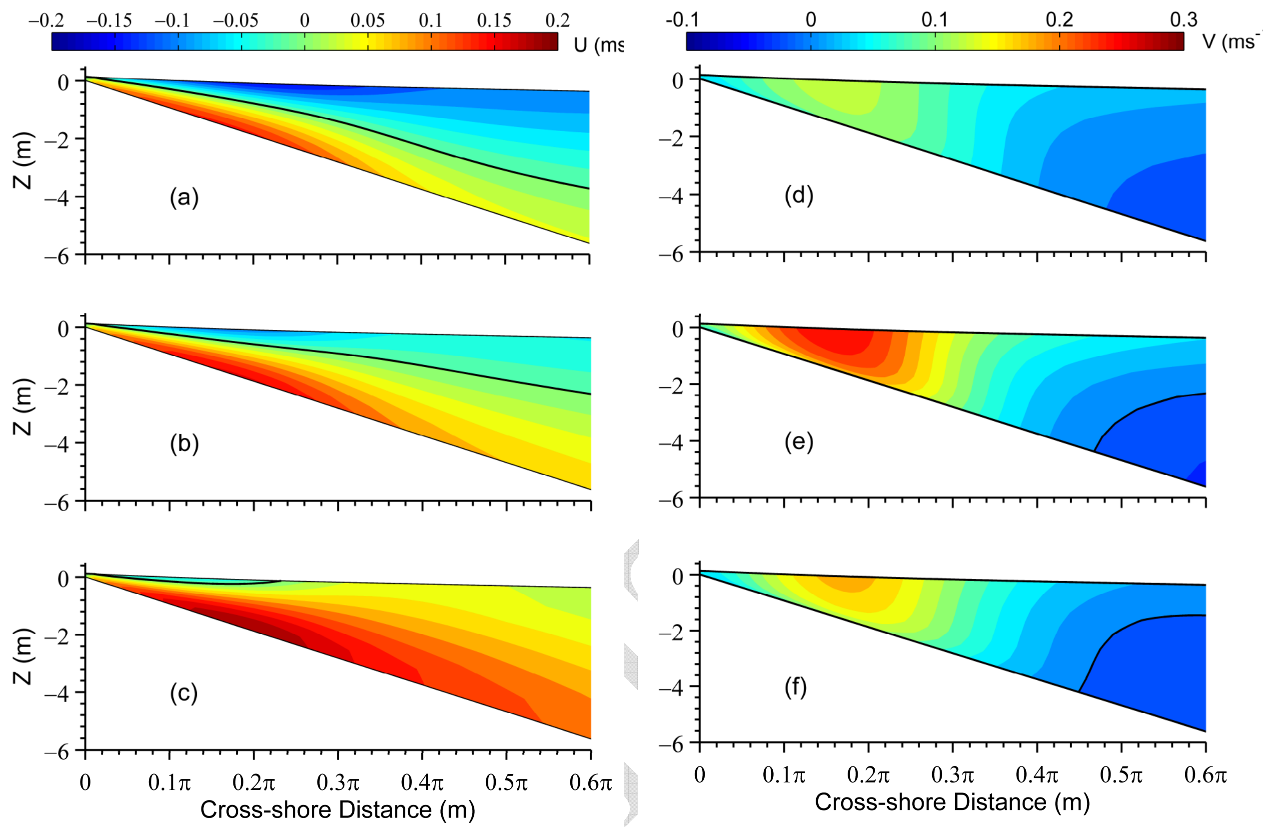

Figure 6. Contour plots showing the vertical structure of the Eulerian cross-shore (a, b, c) and alongshore velocity (d, e, f) along three transects located at λy=π/5 (a, d), λy=π/2 (b, e), and λy=4π/5 (c, f) from the southern lateral boundary (see dashed lines in Figure 3). Solid black line corresponds to zero velocity.

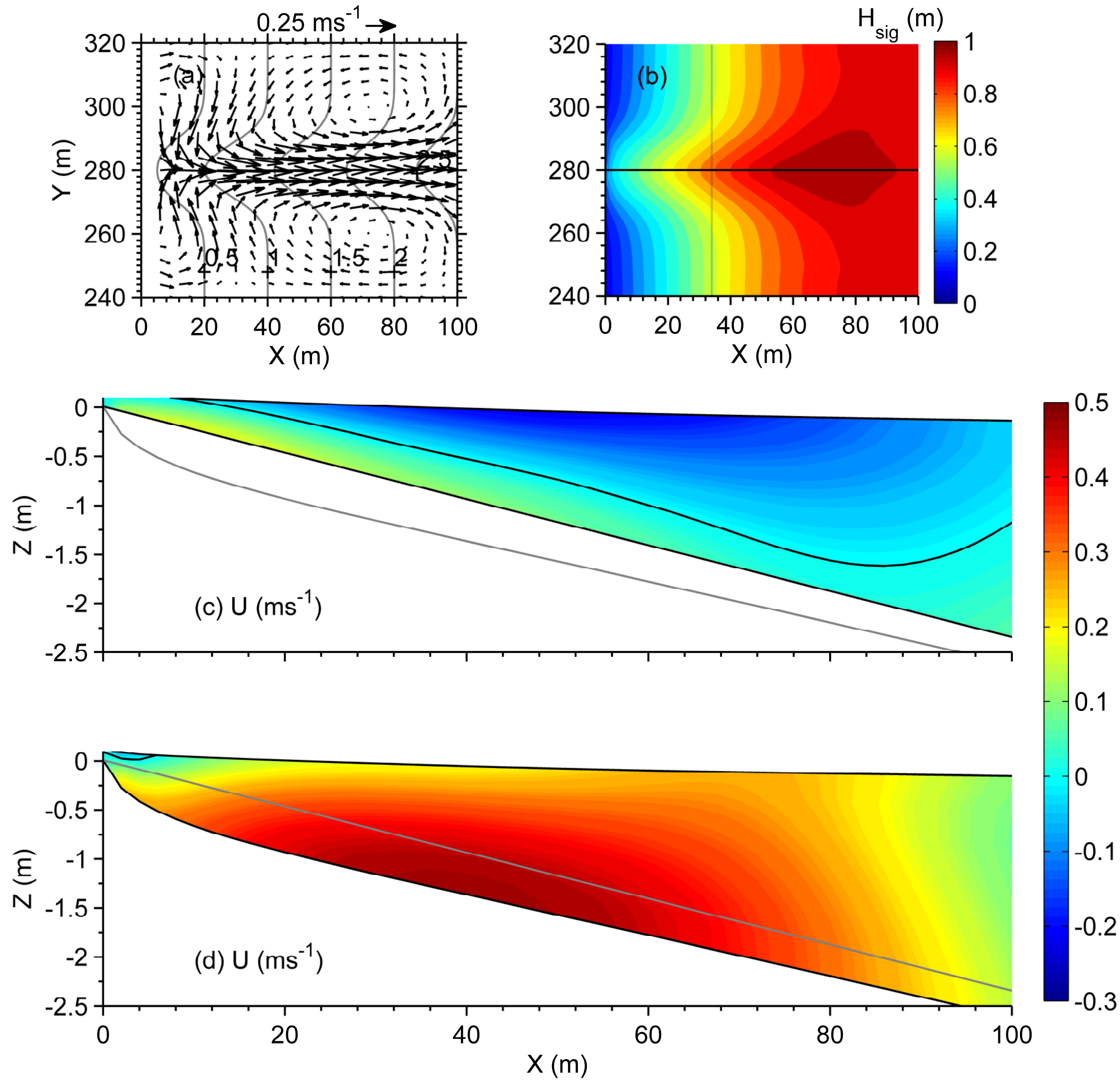

Figure 7. (a) Depth averaged Eulerian velocity (black arrows) after 1 hour of simulation. Light grey lines in background depict the bathymetry contours; (b) Contour of significant wave height distribution over the computational domain. The incident wave height at the offshore boundary of the domain is 0.92 m. Contour plots showing the vertical structure of Eulerian cross-shore velocity, u(x, z) along two transects located at (c) y=0 m, (d) y=40 m from the southern lateral boundary (see grey lines in Figure 7b). The grey dotted alongshore transect in Fig. 7b is location at which alongshore momentum balance term is shown in Fig. 15(c).

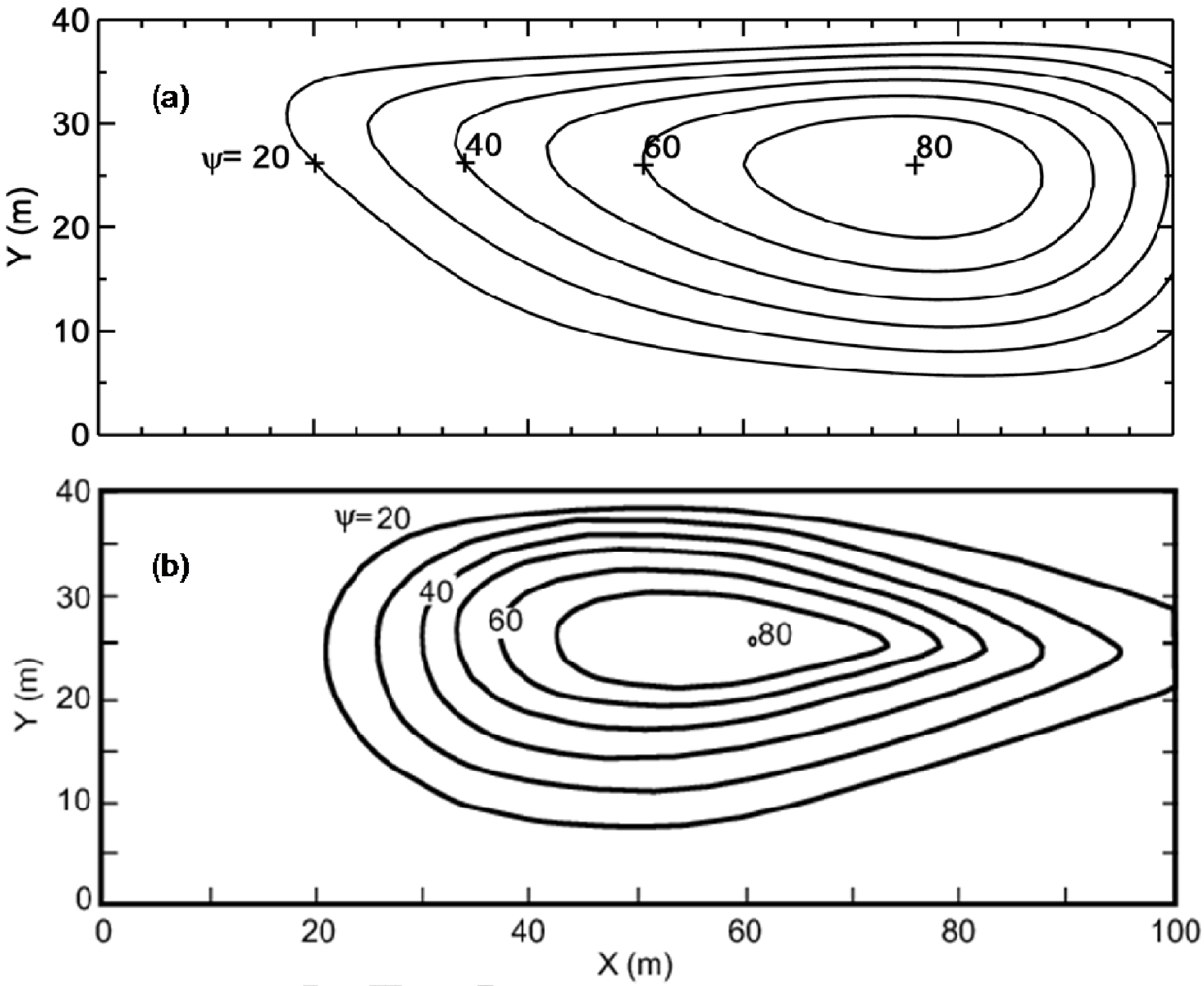

Figure 8. Transport stream function (ψ) over the computational domain computed from the model results after (a) depth averaging the horizontal Lagrangian velocity field; (b) and from Noda (1974) paper.

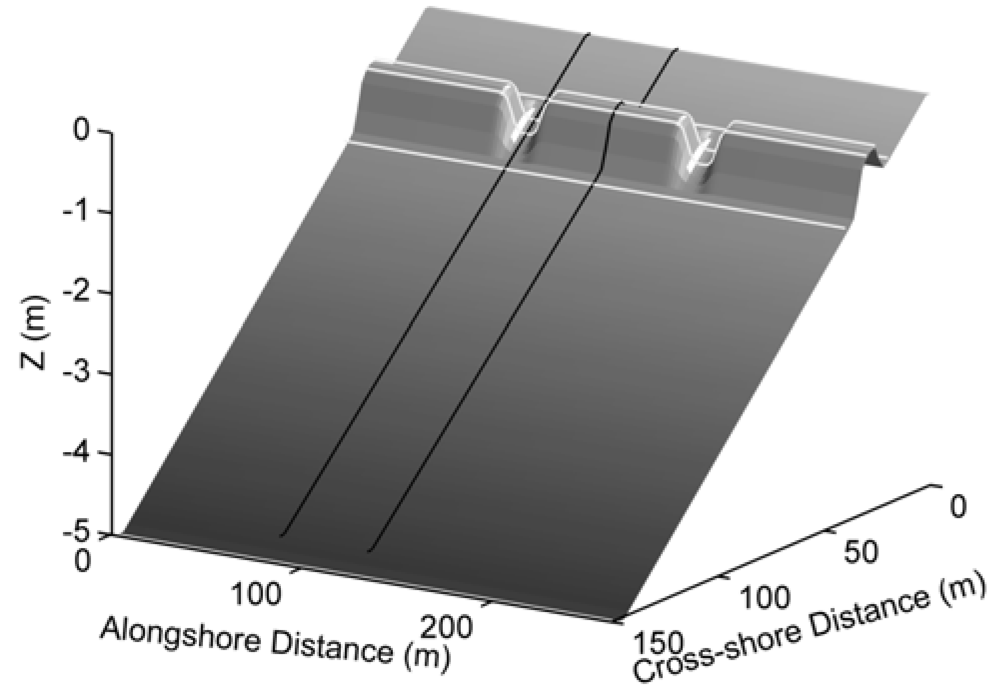

Figure 9. Bathymetry for Case 4, showing the longshore bar and the rip channels. The solid black lines show the location of vertical transects at which the cross-shore velocity distribution is discussed in Fig. 12. The 4 horizontal white lines represent the alongshore transects at which cross-shore momentum balance terms are shown in Fig. 13 and alongshore momentum balance term is shown in Fig. 15(d).

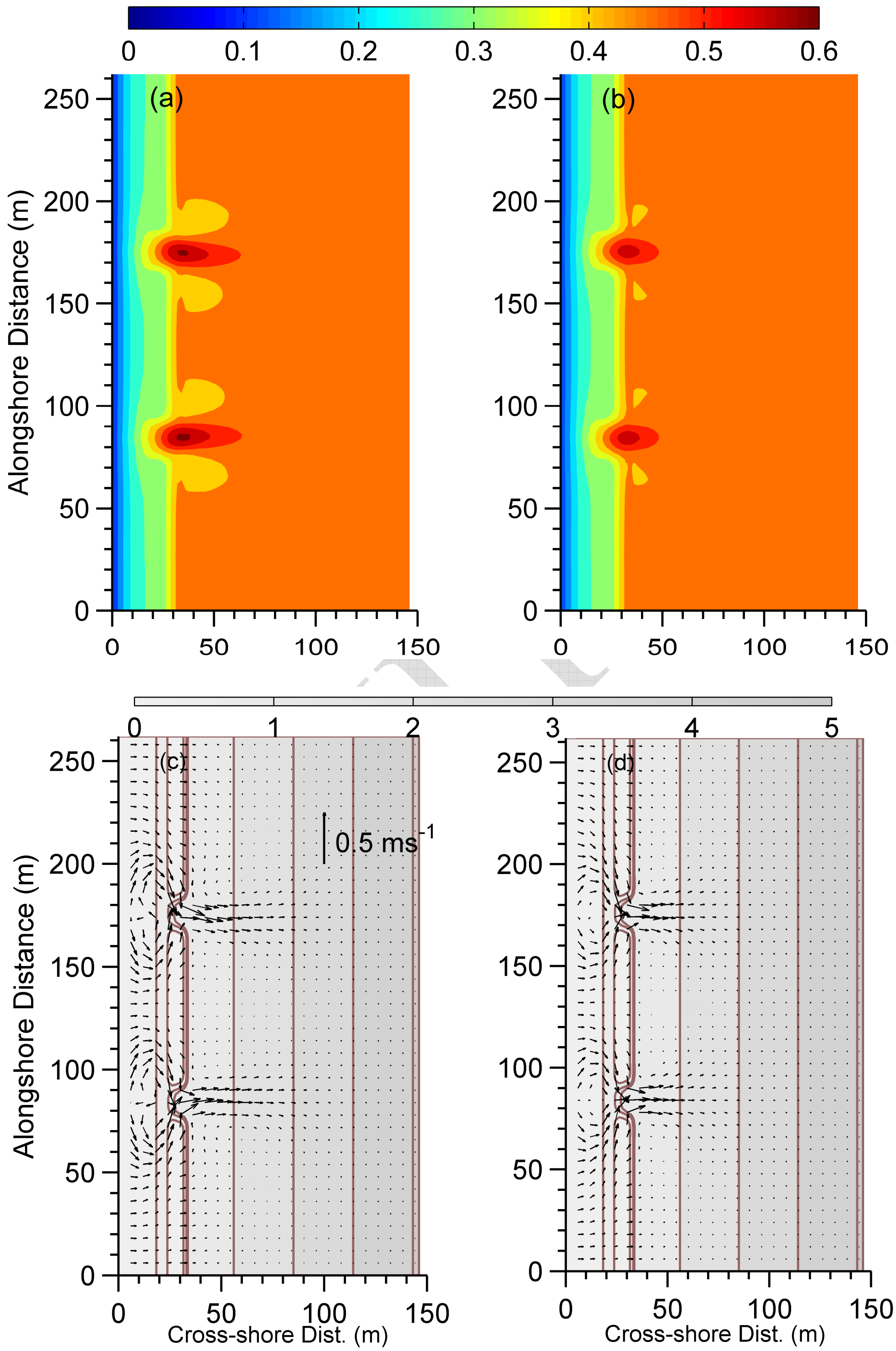

Figure 10. Contours of significant wave height after 30 minutes of model simulation using (a) the original version of the model as in HW09 and; (b) the updated model with the M08 formulations for the vertical distribution of the radiation stress ($M08_{vrt}$). Bathymetric contours

and Eulerian depth integrated mean currents over the computational domain using (c) the original version of the model as in HW09 and; (d) the updated model with the M08 formulations for the vertical distribution of the radiation stress ($M08_{vrt}$). The black line (10c) depicts a velocity of 0.5 ms^{-1}.

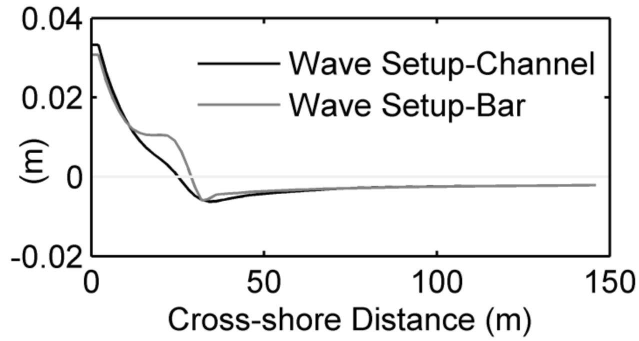

Figure 11. Cross-shore variation of mean sea surface elevation at two locations corresponding to alongshore positions centered at the middle of the rip channel (black) and alongshore bar (grey).

SUBMITTED

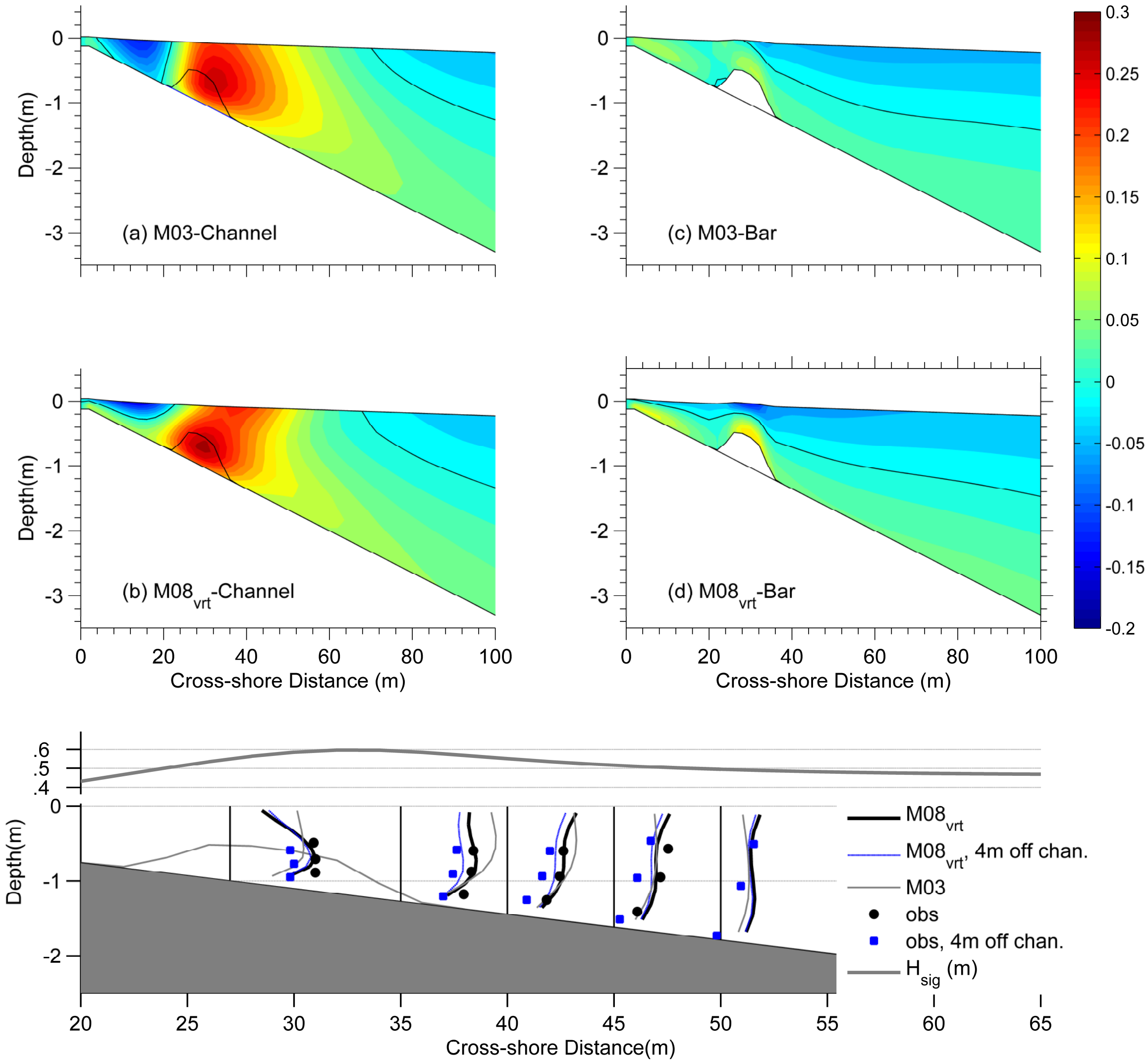

Figure 12. Vertical structure of cross-shore Eulerian velocity u(x,z) at the center of rip channel (a and b) and bar (c and d) derived from original version of the model as in HW09 (a and c) and the updated model with the M08 formulations($M08_{vrt}$) (b and d); (e) Comparison of normalized, model derived cross-shore velocity with normalized data from Haas and Svendsen, 2002 (key: symbols ● and ■ denote data at the center and 0.4m off the channel, grey line (center of the channel M03), black dash dot (center of the channel $M08_{vrt}$), blue dashed line ($M08_{vrt}$, 0.4 m off the channel)).

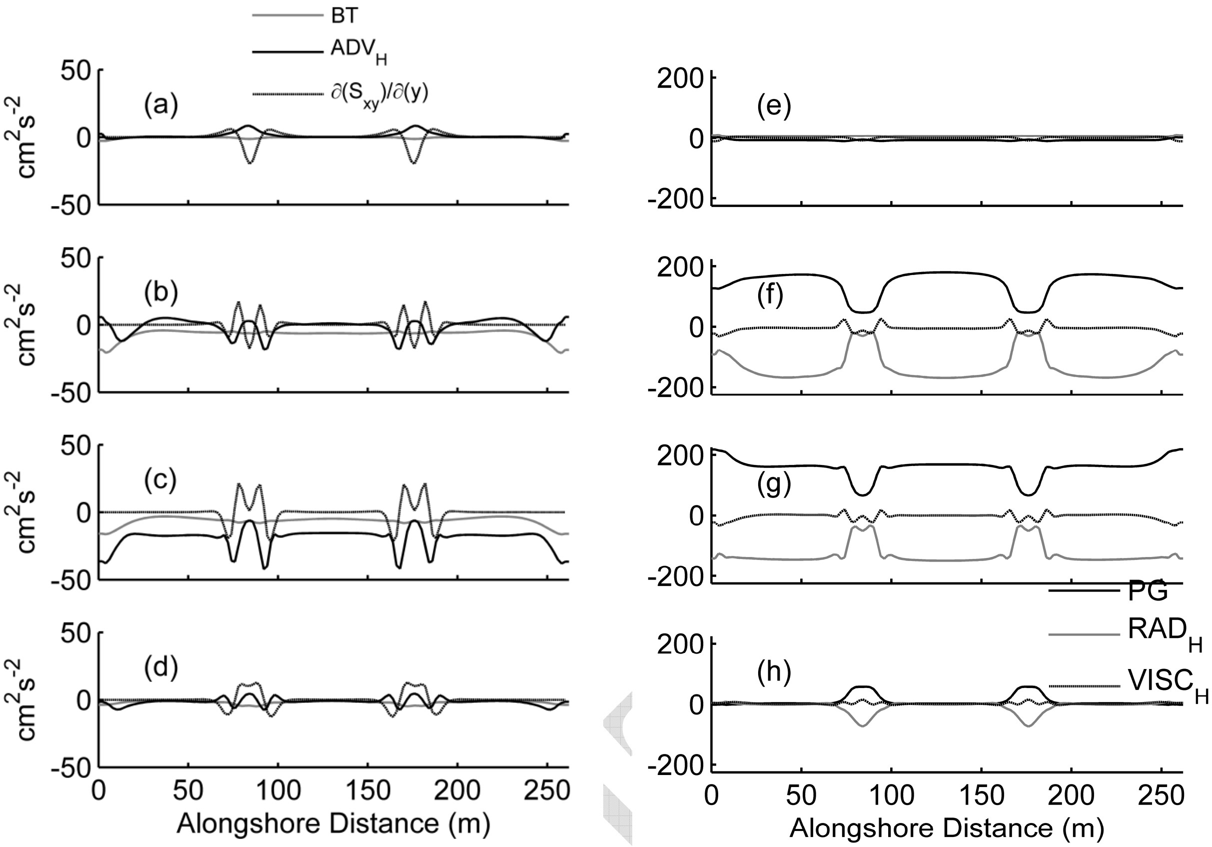

Figure 13. Alongshore variation of the depth averaged cross-shore momentum balance equation terms. Horizontal advection (ADV_H, $\partial/\partial x(U^2h)+\partial/\partial y(UVh)$, black line), bottom stress (BT, τ_x/ρ, grey line) and radiation stress forcing ($\partial S_{xy}/\rho\partial y$, black dashed) terms are shown in (a) to (d). Cross-shore pressure gradient (PG, $gh(\partial\eta/\partial x)$, black line), radiation stress forcing ($\partial S_{xx}/\rho\partial x$, grey line) and horizontal viscosity ($VISC_H$, $\partial(A_H\partial u/\partial x)/(\rho\partial x)$), black dashed) are shown in (e) to (h). The distances at which the terms are estimated are 40 m (a) and (e), 30 m (b) and (f), 26 m (c) and (g), and 20 m (d) and (h) from the shoreline (see Fig. 9).

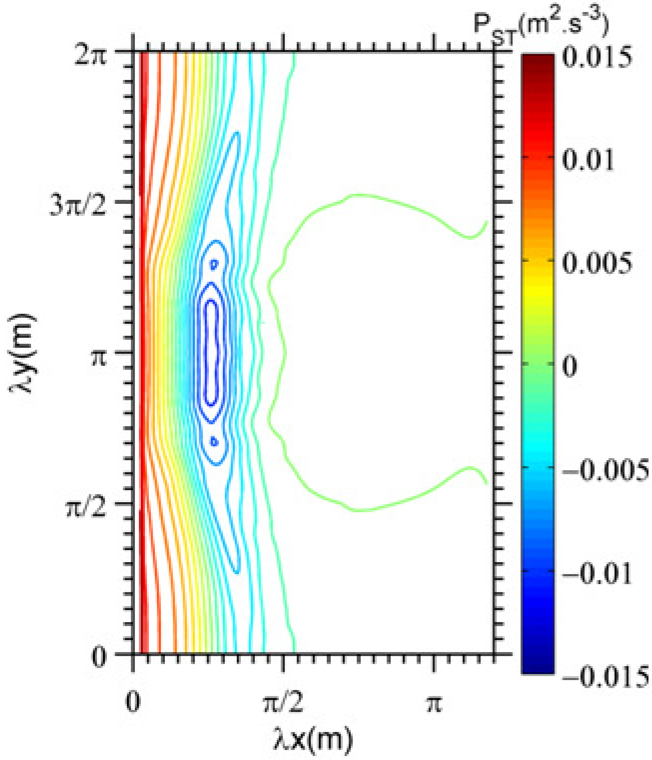

Figure 14. Contour of sediment transport proxy (P_{st}) over computational domain for the run of Case 2 of alongshore variable wave forcing.

SUBMITTED

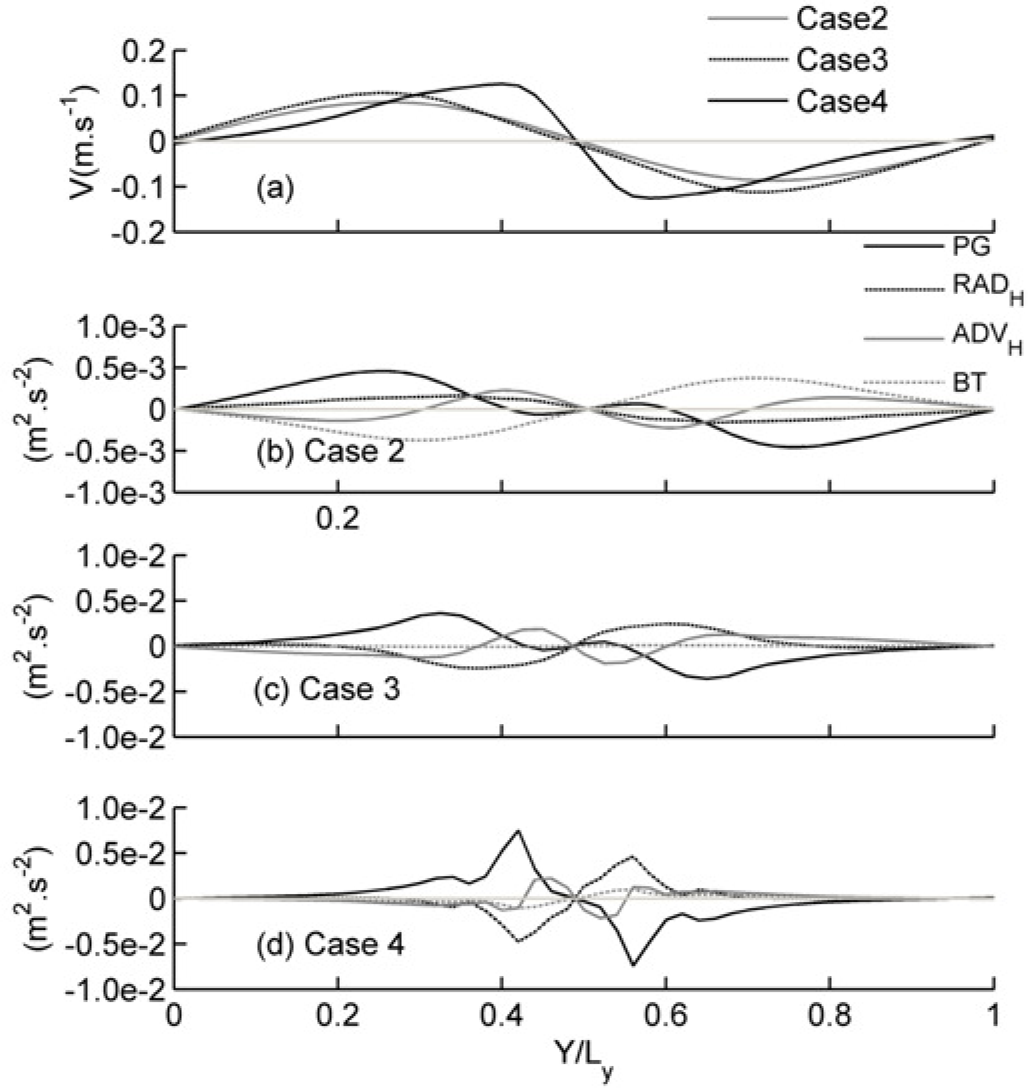

Figure 15. (a) Depth averaged alongshore velocity, V (ms^{-1}) at alongshore transects shown by dotted line in Fig.3 for Case 2, dotted line in Fig.7b for Case 3 and alongshore transect onshore of the rip channel (Fig. 9) for Case 4; Alongshore variation of the depth averaged alongshore momentum balance terms for (b) Case 2 and (c) Case 3 for alongshore transect as 15(a); (d) Case 4 for alongshore transect as 15(a). The alongshore normalizing length scale (L_y) used in (b), (c) and (d) are 1000 m, 80 m and 90 m, respectively, and represent the corresponding perturbation length in forcing or bathymetry (key: alongshore pressure gradient (PG, $gh(\partial\eta/\partial y)$, black line), radiation stress forcing (RAD_H, $(\partial S_{yy}/(\rho\partial y)+\partial S_{xy}/(\rho\partial x))$, black dashed), Horizontal advection (ADV_H, $\partial/\partial x(UVh)+\partial/\partial y(V^2h)$, grey line), bottom stress (BT, τ_y/ρ, grey dashed-dot line)).

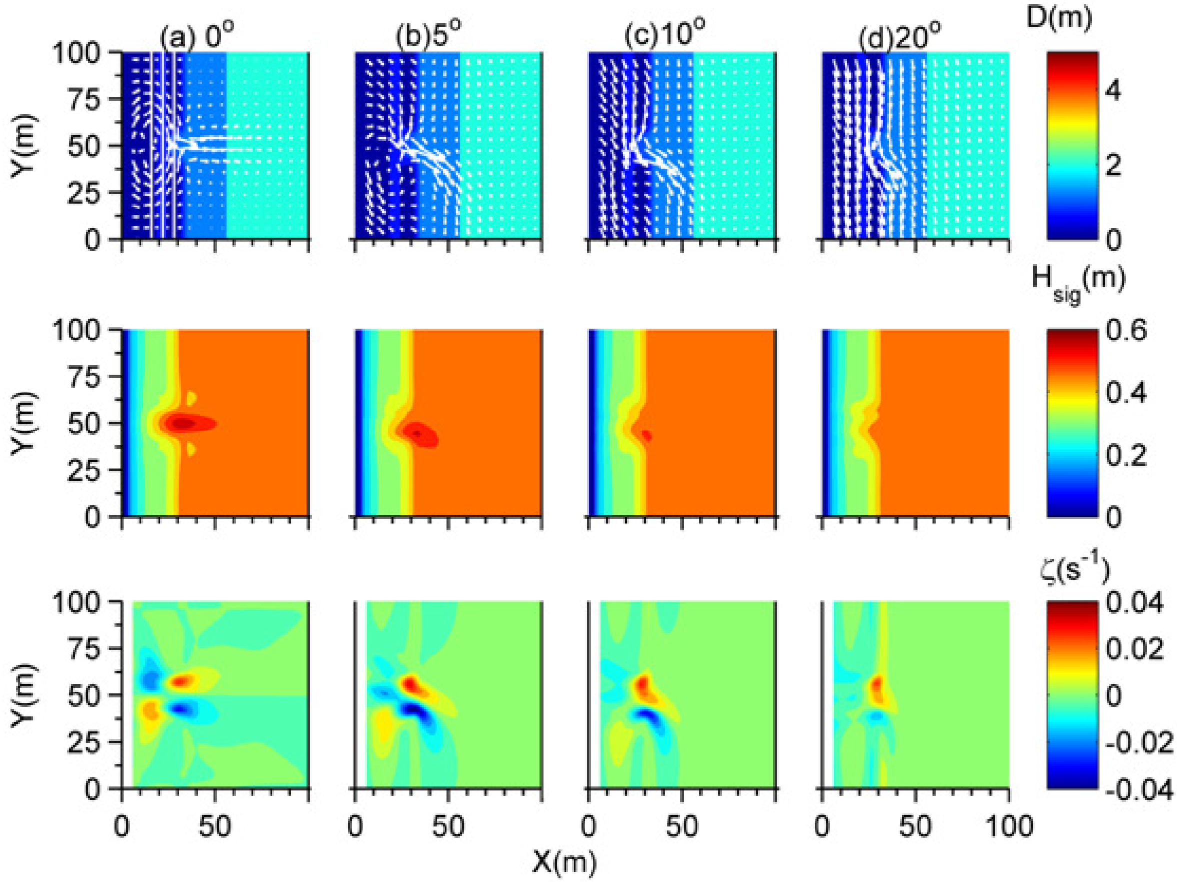

Figure 16. Circulation (depth averaged, Eulerian current vector, top row), significant wave height distribution (middle row) and vorticity field (bottom row) results for different wave incident angles (columns a to d, corresponding to incident angles of 0, 5, 10 and 20 degrees, respectively) The thin grey lines in top row, column (a) show the alongshore transects at which relevant terms are plotted in Figure. 17. Note: The bathymetry used in this case is same as Figure 9, but only the relevant part of the domain is shown here.

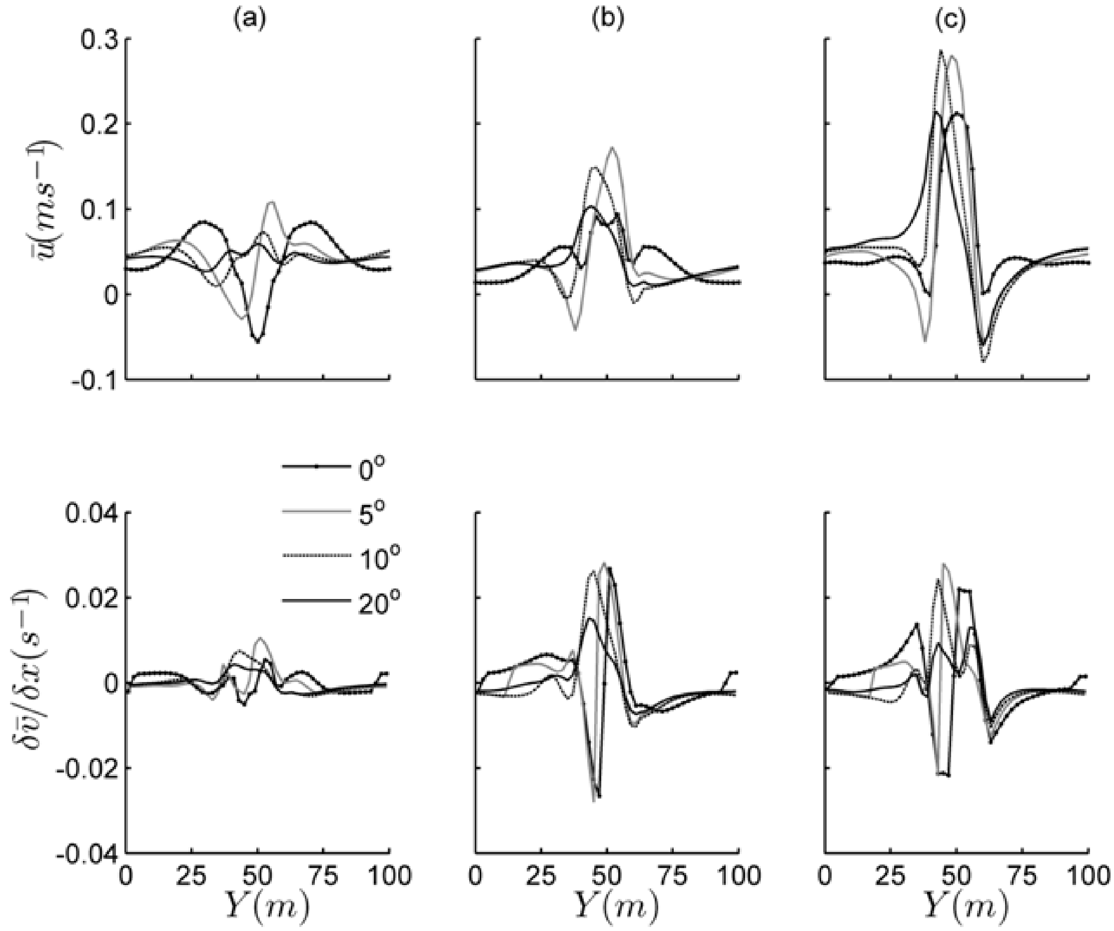

Figure 17. Eulerian cross-shore velocities (top panel) and absolute value of alongshore gradient of Eulerian alongshore velocities (bottom panel) at 3 alongshore transects located (a) 16 m (b) 22 m (c) 28 m from the shoreline as shown by grey lines n Fig. 16 (top panel, column (a)) for waves incident at angles 0^{o}, 5^{o}, 10^{o}, 20^{o} .

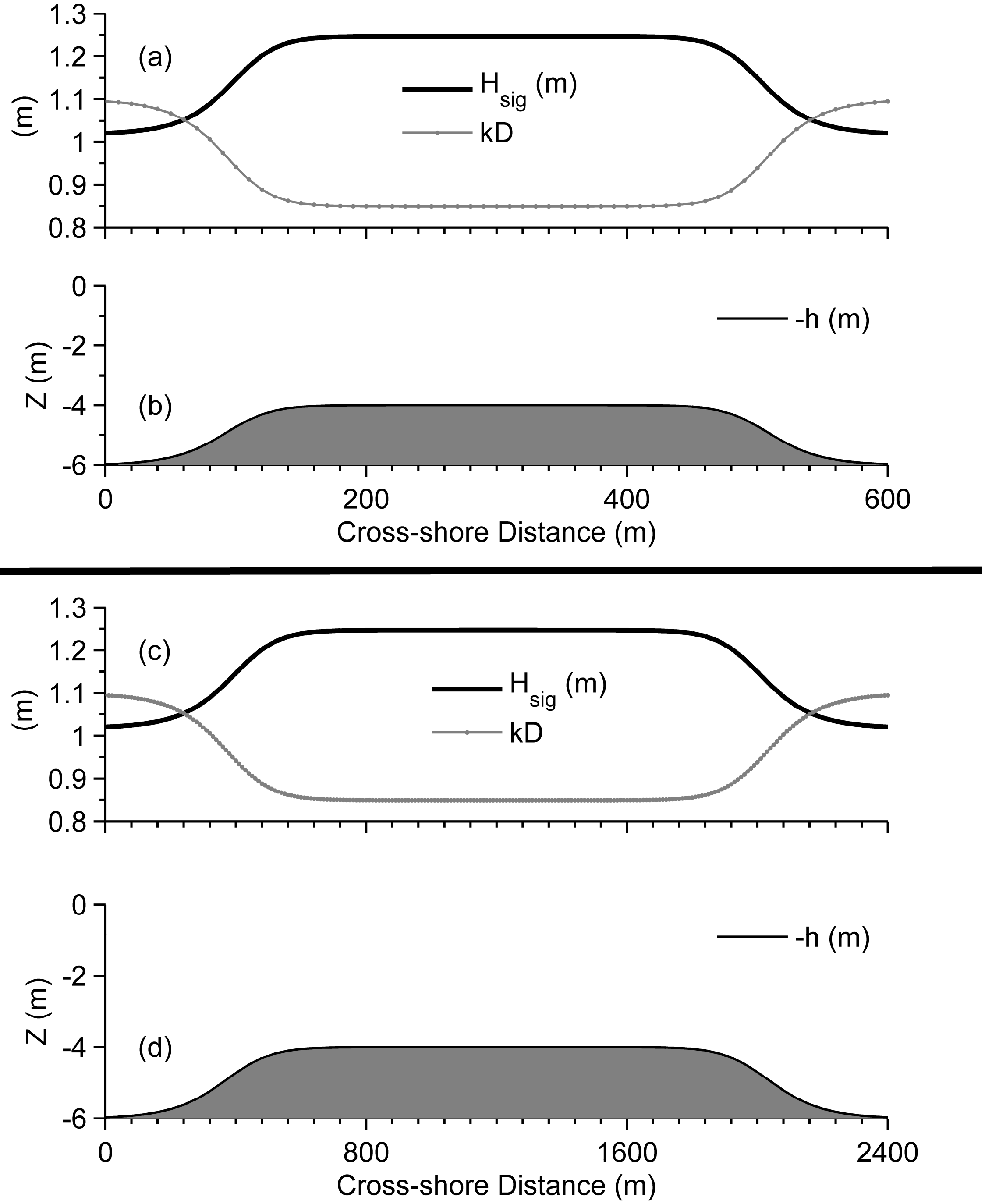

Figure A1. Model forcing (wave height) and non dimensional depth (a and c) and bottom bathymetry (b and d) used to test the Mellor (2008) formulation. (a) and (b) are identical as in Ardhuin et al. (2008). Forcing in (c) is the same as (a) but the bathymetry (d) has a reduced bottom slope (note differences in horizontal scale between b and d).

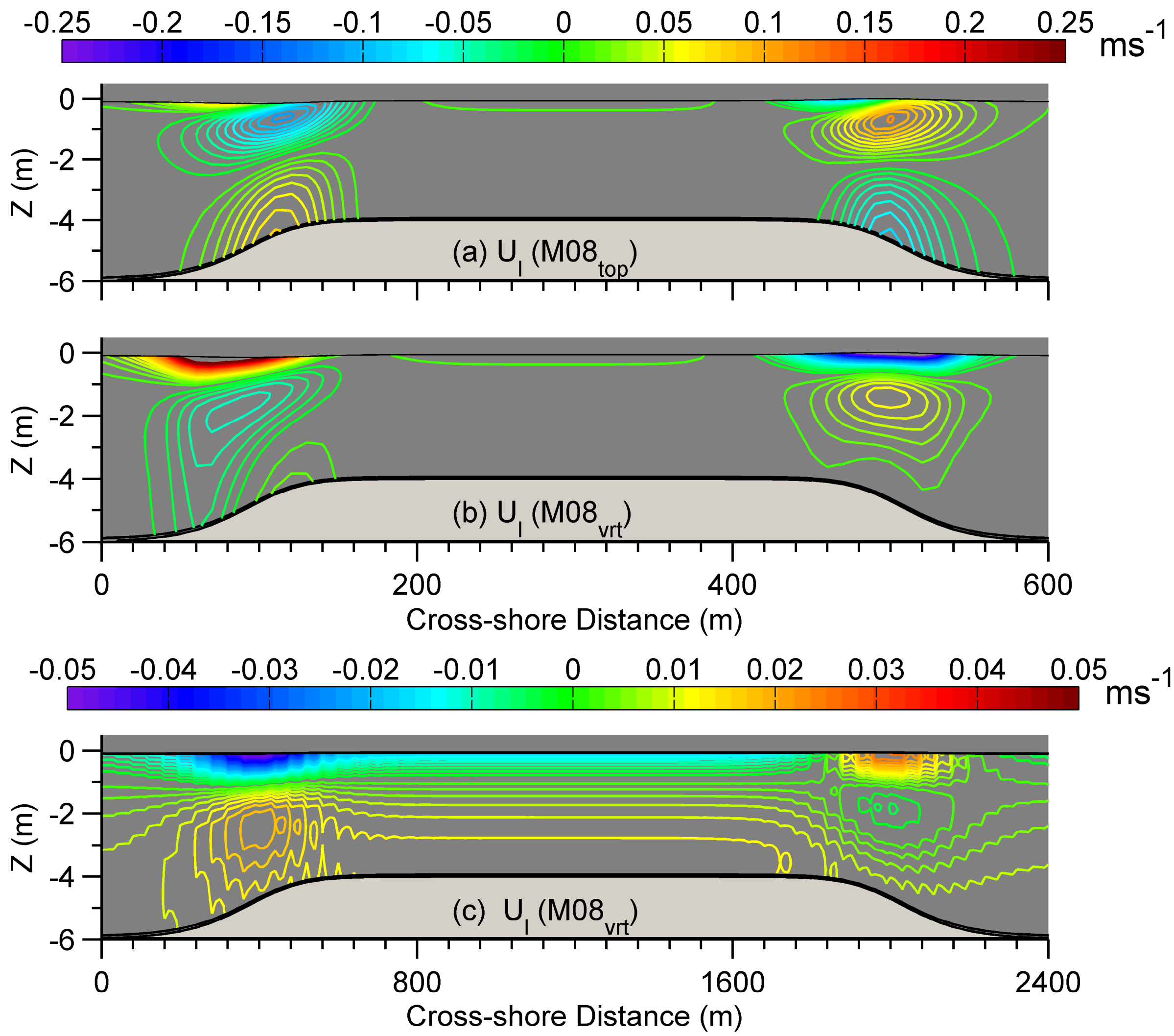

Figure A2. Vertical distribution of Lagrangian velocity, U_l (Eulerian velocity + Stokes drift) calculated using (a) $M08_{top}$ with a domain geometry as in Ardhuin et al. (2008); (b) $M08_{vrt}$ on the same domain as (a); and (c) $M08_{vrt}$ with a similar geometry but reduced bottom slope (note differences in horizontal scale), uniform vertical mixing and bottom friction. Contour line spacing is 0.01 ms^{-1} in (a), (b) and 0.002 ms^{-1} in (c). Note different scales in colorbar used in (c).